ELECTRIC FIELD SENSING USING SINGLE SPIN MAGNET HYBRID SYSTEM

by

Wenqi Tong

A Thesis

Submitted to the Faculty of Purdue University

In Partial Fulfillment of the Requirements for the degree of

Master of Science

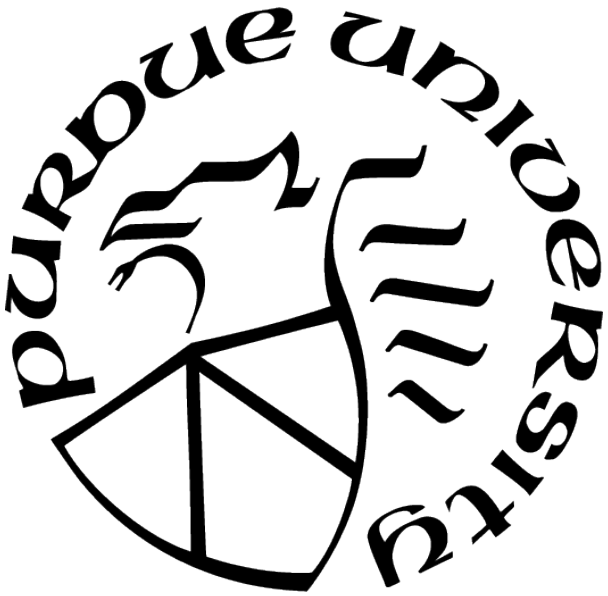

School of Electrical and Computer Engineering

West Lafayette, Indiana

December 2021

THE PURDUE UNIVERSITY GRADUATE SCHOOL
STATEMENT OF COMMITTEE APPROVAL

Dr. Pramey Upadhyaya, Chair

School of Electrical and Computer Engineering

Dr. Mahdi Hosseini

School of Electrical and Computer Engineering

Dr. Shreyas Sen

School of Electrical and Computer Engineering

Approved by:

Dr. Dimitrios Peroulis

To my parents

ACKNOWLEDGMENTS

I would like to thank my advisor, Prof. Pramey Upadhyaya, for his guidance during my Master's study at Purdue. He opens the amazing quantum world for me and offers precious research skills. When meeting challenges and obstacles, his way of thinking and patience provides me with much inspiration and encouragement. In addition to academic activities, he also gives me advice on my future career. He is an outstanding researcher, teacher and mentor. His enthusiasm, curiosity, concentration will influence me through my life.

I also want to deliver my gratitude to my group members, Avinash Rustagi, Abhishek Solanki, Aravindh Shankar, Mohammad Mushfiqur Rahman, and Shiva Konakanchi for their insightful discussion and valuable assistance.

I really appreciate the great help and attention on my thesis that my committee member, Dr. Mahdi Hosseini, Dr. Shreyas Sen have offered.

I would like to acknowledge the staff in ECE department for their administrative and technical help.

Finally, I really want to thank my parents for their continuing support and encouragement throughout my life. I owe everything to them.

TABLE OF CONTENTS

LIST OF TABLES

LIST OF FIGURES

NOMENCLATURE

NV	nitrogen vacancy center
VCMA	voltage-controlled magnetic anisotropy
SQUIDS	superconducting quantum interference devices
SNR	signal-to-noise ratio
FMR	ferromagnetic resonance
SOC	spin-orbit coupling
$L_{\mathrm{i}}(\mathrm{i} = x, y, z)$	dimension of the ferromagnet
PSD	power spectral density
$\vec{E}$	applied electric field
h_{NV}	height of the NV center
$\vec{H}_0$	applied magnetic field
t	evolution time
t_m	initialization and readout time for the NV center
$\vec{m}$	normalized magnetization
$\vec{M}$	magnetization
θ	angle between magnetization and z axis
θ_H	angle between external field and z axis
$\mathcal{F}$	free energy of the ferromagnet
M_s	saturation magnetization
K	anisotropy energy corresponding to H_k
H_k	anisotropy field along z axis
$H_\perp$	anisotropy field along x axis
$\vec{H}_{eff}$	effective magnetic field
γ	gyromagnetic ratio
$R_y(\theta)$	operator for clockwise rotation about y axis by θ
ω_{FMR}	ferromagnet resonance frequency
α	Gilbert damping coefficent
$\vec{h}$	thermally excited noisy magnetic field

$S_{\mathrm{ij}}(\mathrm{i},\mathrm{j}=x,yz)$	susceptibility matrix element
D_{th}	correlation function of thermal field $\vec{h}$
C_{ij}	correlation function of i and j components of magnetization deviation
$\vec{B}$	magnetic induction intensity
$\vec{\nabla}$	gradient vector operator
Φ	scalar potential for finding stray field
$B_{\mathrm{j}}^{\mathrm{i}}$	stray field matrix element
$\vec{H}$	total field at the NV center
NV	nitrogen-vacancy center
$\left\|0\right\rangle_g, \left\|\pm1\right\rangle_g, \left\|0\right\rangle_{\mathrm{e}}, \left\|\pm1\right\rangle_{\mathrm{e}}, \left\|s\right\rangle$	quantum states of the NV center
m_s	spin quantum number
$\mathcal{H}$	Hamiltonian
D_{nvg}	zero field splitting between $\left\|0\right\rangle_g$ and degenerate $\left\|\pm1\right\rangle$
$\vec{S}$	spin vector operator
$\epsilon_z, \epsilon_{xy}$	NV's coupling strength to longitudinal and transverse electric field
$P_{0\to-1}$	transition probability from $\left\|0\right\rangle_g$ to $\left\|-1\right\rangle_g$
$\tilde{K}(\omega)$	a measure of power density spectrum of magnetic field at NV
Γ	transition rate related to T_1 time
ϵ	energy splitting between $\left\|0\right\rangle_g$ and $\left\|-1\right\rangle_g$
p_0	population of $\left\|0\right\rangle_g$
K_{i}	interfacial anisotropy energy
β	VCMA coefficient
ξ	conversion coefficient from electric field to magnetic anisotropy
λ_s	saturation magnetostriction
Y	Young's Modulus
d_{eff}	effective piezomagnetic coefficient
δp	population difference
N	total measurement counts
σ_p	standard deviation of p

κ	ratio of wrong assignment
σ_x	photon shot noise
C	overall readout efficiency

ABSTRACT

Quantum sensing, a protocol that takes advantage of the extreme sensitivity of quantum systems to their environment, enables many applications of quantum systems for sensing. Inspired by direct electric field sensing using the Stark effect of a nitrogen-vacancy(NV) center, this work implements an NV-magnet hybrid way to explore the possibilities of overcoming NV's relatively weak coupling strength to electric fields. The magnetic-noise-induced population relaxation of the NV center serves as the mechanism for sensing. Within this scheme, the magnetic noise spectrum is tuned by modulating the magnetic properties via voltage-controlled magnetic anisotropy (VCMA) or electric-field-induced magnetoelastic effect. In this way, the noise carrying the information of the electric field is taken as a signal - the shift of the noise spectrum leads to a population difference of NV energy levels, which is used for evaluating electric fields. The investigation of the relation between sensitivities and operation points reveals that lower operation frequency is desirable for better performance. The comparison between VCMA and electric-field-induced magnetoelastic effect indicates that the efficiency of converting electric field into magnetic property modulation is a critical parameter for sensitivity enhancement.

1. INTRODUCTION

Since Willard Boyle and George E. Smith proposed the charge-coupled device (CCD) as an image sensor, it has become a major photosensitive element in many digital cameras[1]. Measuring the temperature of digital devices allows studying the temperature-dependent performance of electronic devices. Nowadays, people can use the silicon bandgap temperature sensor to monitor the states of electronic equipment[2]. In biomedical research, electric field sensors are employed to investigate activities in a living cell[3]. Sensors, detecting and converting physical quantities into signals people can handle, have played an increasingly important role in our lives. Frequently people employ classical systems for sensing, while in recent decades, quantum systems have emerged as a promising alternate[4]. Quantum systems are notoriously vulnerable to external disturbances. For example, the longitudinal and transverse noise may result in the loss of population and phase information, characterized by T_1 and T_2 time, respectively[5][6]. However, if we think another way, does "vulnerable" also mean "sensitive"? What if the perturbations are exactly or associated with physical quantities interested? Can we utilize such a property of quantum systems for sensing?

In recent years people are making enormous efforts to develop various quantum sensors:

1. Atomic vapors, spin-polarized by a pumping laser, rely on coherent precession about the external magnetic field for sensing[7]. Due to the relaxation and decoherence time up to second or even minute range[8], atomic vapors prove to be outstanding magnetic field sensors, with sensitivities to the order of $\sim 100aT/\sqrt{Hz}$ [9][10]; however, as for imaging applications, the spatial resolution is limited due to their finite volume (down to mm^3)[11].

2. Trapped ions, whose quantized motional levels are strongly coupled to electric fields, are predicted with sensitivities of $500nV/(cm \cdot \sqrt{Hz})$ for electric fields and $1yN/\sqrt{Hz}$ for force sensing[12][13]. Meanwhile, as magnetic field sensors, trapped ions demonstrate the sensitivity of $4.6pT/\sqrt{Hz}$[14]. Due to the tiny size of single-trapped-ion magnetometers, they have the potential for high-resolution applications such as magnetic microscopy[15]. However, to "trap" the ions, a delicate magnetic or electric potential and laser cooling are

required, leading to a complicated lab configuration[16]. As a result, how to operate trapped ions in close proximity to sample surfaces remains challenging[15].

3. Superconducting quantum interference devices (SQUIDs), whose loop phase is extremely sensitive to the external magnetic flux, are comparable magnetometers to atomic vapors with a sensitivity of $\sim 10aT/\sqrt{Hz}$[17][18]. SQUIDs miniaturized to submicron size allow nanoscale magnetic imaging[19]. However, as probes SQUIDs may be perturbative, and the low-temperature requirement restricts their application range[20].

Assembling many advantages of existing quantum sensors, the Nitrogen-vacancy color center in diamond (NV center) has emerged as a competitive candidate for sensing. Specifically, NV centers are promising for several reasons:

1. Thermal stability enabling operation under temperatures from $\sim 10mK$ to $\sim 600K$ - wider range allows more potential applications and simplified room-temperature lab configuration[21][22][23].

2. Nanoscale resolution - the resolution of the NV sensor is governed by how close the NV can be brought into the target. The NV center can be located in the depth of $\sim 2nm$ from the diamond surface, facilitating detection in very close proximity to the sample[24][25].

3. Non-perturbative operation - the NV center does not carry significant magnetic moments or moving charges that may generate a non-negligible stray field at the sample, which gives more reliable measurements[20].

4. Low cytotoxicity - the NV center is reported to be non-toxic in a living cell, making the i*n vivo* observation of cell activities possible[26].

5. Unlimited photostability ($> days$) - the fluorescence emission spectrum of the NV center shows no detectable change with time, which is desirable for optical readout and fluorescence labeling[24][27][28].

6. Moderate sensitivity to magnetic fields - the NV center couples to magnetic fields by Zeeman effect with strength characterized by the gyromagnetic ratio $\gamma = 2.8MHz/G$[24]. The NV ensemble is reported with the sensitivity of $\sim 1pT/\sqrt{Hz}$ [29], while the single NV reaches $\sim 1\mu T/\sqrt{Hz}$ for dc magnetic fields and $\sim 100nT/\sqrt{Hz}$ for ac fields [30][31][32].

Despite the inferior sensitivity of magnetic fields compared to the atom vapor cell or SQUIDs, other strengths of NV centers make them versatile and convenient sensors with

applications in quantum optics, bio labeling, condensed matter physics, and so on. However, compared to magnetic sensing, the coupling of NV ground states to electric fields is not as strong[33]. Since the single NV center was proposed as an electric field sensor with sensitivity $202V/(cm \cdot \sqrt{Hz})$ for ac and $891V/(cm \cdot \sqrt{Hz})$ for dc electric fields[34], people have been making efforts to enhance the sensitivity:

By using a $1ppm$ NV ensemble, Chen *et al.*,[35] investigate the Stark effect on hyperfine states of NV centers, demonstrates the sensitivity of $\sim 1V/(cm \cdot \sqrt{Hz})$, and predicts that by using the NV ensemble with higher density, the sensitivity may approach $6 \times 10^{-3}V/(cm \cdot \sqrt{Hz})$. Instead of using Stark effect of ground triplet, Block *et al.*,[36] take the ^3E excited states into account - by *on resonance* optical pumping and looking at the gap shift between excited states and ground states, Block *et al.*,[36] figure out the electric field susceptibility of the excited states $\chi^e_\perp = 1.4MHz/(V/m)$ and $\chi^e_\parallel = 0.7MHz/(V/m)$ with sensitivity $1.3mV/(cm \cdot \sqrt{Hz})$. However, the cryogenic temperature $< 45K$ is required since the temperature-dependant optical transition linewidth should be less than the zero field splitting[36].

Another problem of the Stark-effect-based sensing lies in the perturbative effects caused by the magnetic field since the coupling strength to magnetic fields is relatively stronger and may overwhelm the Stark effect. In [34] and [37], the axial magnetic field is suppressed by applying a transverse magnetic field, while in [38], an engineered continuous driving microwave is introduced to construct a new dressed state basis with zero expectation of the spin operator but maximized expectation value of the dipole operator, leading to a suppression of the axial magnetic field and the preserved Stark effect.

Overall, it is still challenging to improve electric field sensitivity by directly coupling to NV centers via the Stark effect. In this work, we present an indirect way (using the Zeeman effect) to sense electric field: By converting the electric field into the shift of power spectral density of magnetic noise generated at the NV center, the electric field can be detected optically, taking advantage of the well-established high sensitivity of NV center to magnetic noise. Without complicated manipulation pulse sequences and the cryogenic temperature requirement, the sensing procedure and platform can be very simple. Besides, the absence of the microwave also results in lower power consumption. The scheme of conversion from

electric fields to magnetic noise opens a new possibility to enhance the electric field sensitivity by improving the efficiency of such transformation.

This work is organized as follows: in the theory chapter, we give the configuration of the sensing platform, the theories for the NV-magnet hybrid sensing, and the sensitivity evaluation. The methodology chapter will exhibit some details of the simulation and the parameters involved. Then we will show some simulation results and discuss the possibility of choosing better operation points and materials with better electric-to-magnetic conversion. Finally, we conclude our work and give some outlook for future research in this area.

2. THEORY

In this chapter, the configuration of the sensing platform, the theory of the electric field sensor, and derivation of the sensitivity will be elaborated.

The setup of the sensor is shown in Figure 2.1, consisting of 2 blocks: A single-domain magnet with size (L_x, L_y, L_z) is located on a substrate with thickness of t_{ox}, applied a DC electric field of E along x direction. Above the magnet by h_{NV} lies the single NV center positioned at $(x = h_{NV}, y = L_y/2, z = L_z/2)$. The system works at room temperature where $T = 300K$. For simplicity, the easy axis, external magnetic field and orientation of the NV center are along the z-axis.

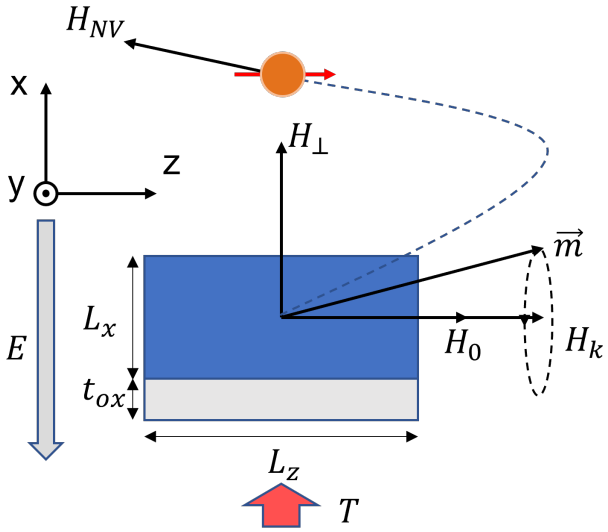

Figure 2.1. Configuration of the sensor

Figure 2.2 shows the pulse sequence, the sensor is manipulated (doing readout and initialization) for t_m, evolves for t and then repeats the manipulation and evolution for time T_{tot} in total. In this work, we use $t_m = 10\mu s$, a typical value for NV initialization and readout. Equivalently, the number of measurements is $N = \frac{T_{tot}}{t+t_m}$ and we will take the average of those measurements as the result.

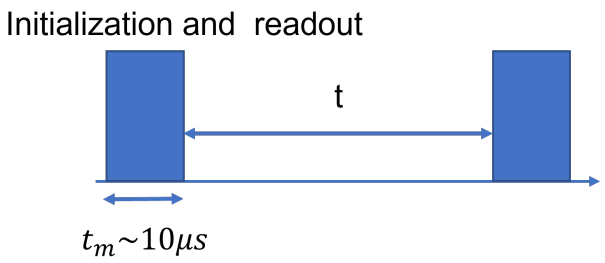

Figure 2.2. Pulse sequence of manipulation and evolution

The central idea of this work is illustrated in Figure 2.3. The sensor comprises two parts - the magnet part and the NV part. For the magnet part, the electric field modulates the power spectrum of the magnetic noise, which can be equivalently considered as the electric-field-induced shift of ferromagnetic resonance (FMR) frequency[39], corresponding to the parameter $\frac{d\omega}{dE}$ we will discuss later. For the NV part, the NV center experiences the magnetic noise with shifted power spectrum and exhibits a different transition rate, which can be considered as the difference of the NV's transition rate due to the shift of ω_{FMR}, corresponding to the parameter $\frac{d\Gamma}{d\omega}$.

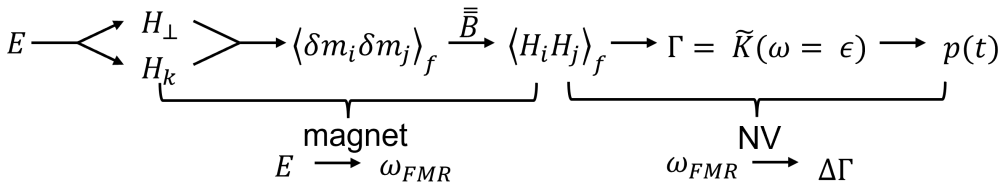

Figure 2.3. Central idea of this work - the electric-field-induced magnetic anisotropy modulation propagates to the population dynamics

In the following sections:

1. We first investigate the magnetization dynamics induced by an effective fluctuating field due to the finite temperature, introducing the power spectrum of the magnetization.

2. And then by solving the stray field, we can see how such noisy magnetization couples to the noisy magnetic field at the NV center and results in population relaxation of the NV center, including the evaluation of the transition rate (probability of transition for a unit population in unit time) and the corresponding population dynamics.

3. Finally, we will study how the input of the system (the electric field) yields the output (the population different) as illustrated in Figure 2.3: The electric field applied modulates the magnetic anisotropy ($H_\perp$ and H_k), rendering shifted power spectral density (PSD) of the magnetization as well as the stray field felt by the NV center. As a result, the NV center demonstrates different relaxation rates and hence experiences different population dynamics. By comparing the population difference, one can detect the electric field indirectly.

2.1 Magnetization dynamics

2.1.1 Equilibrium

We start from the system without the electric field. The state of the magnet is described by the normalized dimensionless magnetization $\vec{m}$. To study the dynamics, we shall first analyze its equilibrium. A ferromagnet with an external field $\vec{H}_0$ applied is shown in Figure 2.4. The angle between the external field and the z-axis is θ_H while the angle between the magnetization $\vec{m}$ and the z-axis is θ. Typically a system reaches its equilibrium when its energy is minimal. Determining equilibrium means to obtain the θ that minimizes the free energy of the magnet given by[40]:

$$\mathcal{F} = -M_s \vec{m} \cdot \vec{H}_0 - K m_z^2 + \frac{M_s}{2} H_\perp m_x^2 \tag{2.1}$$

Here M_s is the saturation magnetization. K is the anisotropy constant associated with

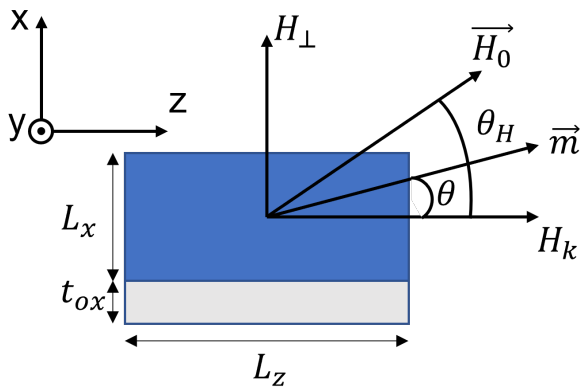

Figure 2.4. The equilibrium magnetization of a ferromagnet in an external field

the z-axis, describing how much energy we need to pay to rotate the magnetization from the z-axis by applying a transverse magnetic field at least $H_k = \frac{2K}{M_s}$. $H_\perp$ is the effective perpendicular anisotropy field defined similarly to H_k except for the direction (the x-axis). m_z and m_x denote the correspondent magnetization component in z and x directions.

The effective field considering the external field and anisotropy field can be obtained by the derivative of $\mathcal{F}$ in terms of the magnetization:

$$\vec{H}_{eff} = -\frac{1}{M_s}\frac{d\mathcal{F}}{d\vec{m}} = \vec{H_0} + H_k m_z \hat{z} - H_\perp m_x \hat{x} = \begin{bmatrix} H_0 \sin\theta_H - H_\perp m_x \\ 0 \\ H_0 \cos\theta_H + H_k m_z \end{bmatrix} \tag{2.2}$$

where $\hat{z}$ and $\hat{x}$ are the unit vector along z and x directions. The effective field points out the orientation for magnetization to reduce free energy in the fastest way. Now with the free energy and effective field we can evaluate the equilibrium orientation of $\vec{m}$ by looking for the minimum value of the free energy:

$$\frac{d\mathcal{F}}{d\theta} = 0 \tag{2.3}$$

We obtain:

$$\sin 2\theta = \frac{2H_0}{H_k + H_\perp}\sin(\theta_H - \theta) \tag{2.4}$$

Substituting the magnitude of the external field H_0 and the effective anisotropy field H_k (along the z-axis) and $H_\perp$ (along the x-axis) we obtain in the following derivation, we can check that $\theta = 0$, that is, the equilibrium of $\vec{m}$ is along the z-axis.

2.1.2 Dynamics

Having solved the steady-state, we may wonder if we deviate $\vec{m}$ from its equilibrium by $\delta\vec{m}$, what would be its dynamics. The Landau-Lifshitz equation (LL) dominates the motion of the magnetization without damping[40]:

$$\frac{d\vec{m}}{dt} = -\gamma\vec{m} \times \vec{H}_{eff} \tag{2.5}$$

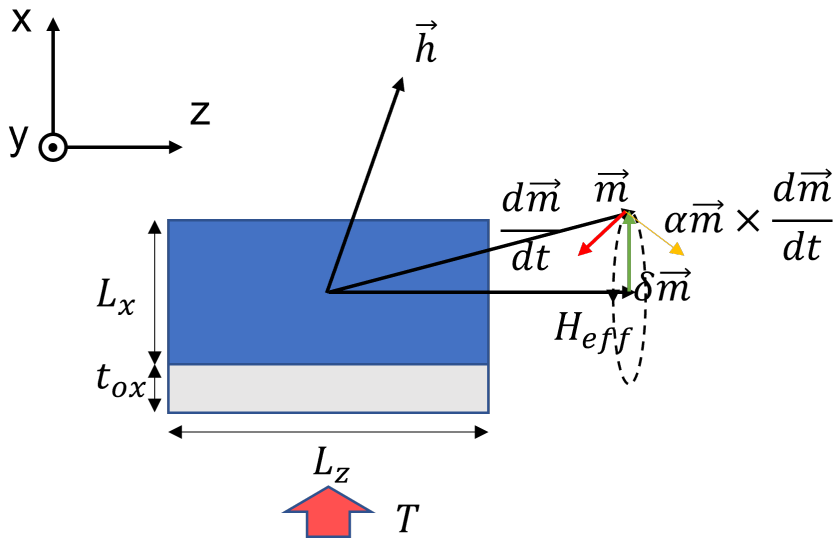

Figure 2.5. Illustration of the LLG equation, considering the dissipation and temperature-induced fluctuating field

where γ is the gyromagnetic ratio. By looking at equation 2.5 and Figure 2.5, we find that the time derivative of $\vec{m}$ is always perpendicular to the effective field $\vec{H}_{eff}$ and $\vec{m}$ itself. So we can expect that $\vec{m}$ is precessing about $\vec{H}_{eff}$ and the rotation frequency (ferromagnetic resonance frequency, FMR), related to γ and $\vec{H}_{eff}$, is what we are interested.

To simplify the solving procedure, we: 1. linearize the LL equation; 2. use the magnet frame.

Linearization of LL equation means that we decompose $\vec{m}$ into its equilibrium $\vec{m}_{eq}$ and deviation $\delta\vec{m}$, $\vec{H}_{eff}$ into $\vec{H}_{eff,eq}$ and $\delta\vec{m}$-induced $\delta\vec{H}_{eff}$:

$$\frac{d\vec{m}_{eq}}{dt} + \frac{d\delta\vec{m}}{dt} = -\gamma(\vec{m}_{eq} + \delta\vec{m}) \times (\vec{H}_{eff,eq} + \delta\vec{H}_{eff}) \tag{2.6}$$

We are only interested in the dynamics of $\delta\vec{m}$ since the dynamics of the equilibrium $\frac{d\vec{m}_{eq}}{dt}$ is literally zero and the cross product $\vec{m}_{eq} \times \vec{H}_{eff,eq}$ is also zero because $\vec{m}_{eq}$ and $\vec{H}_{eff,eq}$ are parallel to minimize the free energy. One can check this by letting:

$$\tan\theta = \frac{\sin\theta}{\cos\theta} = \frac{H_{eff,eq,x}}{H_{eff,eq,z}} \tag{2.7}$$

and will end up with equation 2.4. In addition, the higher order term $\delta\vec{m} \times \delta\vec{H}_{eff}$ is omitted assuming that $\delta\vec{m}$ is very small and the $\delta\vec{m}$-induced $\delta\vec{H}_{eff}$ is tiny (refer to equation 2.13), too. So the linearized LL equation reads:

$$\frac{d\delta\vec{m}}{dt} = -\gamma\vec{m}_{eq} \times \delta\vec{H}_{eff} - \gamma\delta\vec{m} \times \vec{H}_{eff,eq} \tag{2.8}$$

The magnet frame, obtained by rotating the lab coordinate system about the y-axis by θ, aligns the z-axis to the equilibrium magnetization to simplify the representation of $\vec{m}_{eq}$. Here we denote all the variables in the magnet frame by adding a prime ($\prime$) to its notation in the lab frame. The clockwise rotation about the y-axis by θ can be represented by the operator:

$$R_y(\theta) = \begin{bmatrix} \cos\theta & 0 & \sin\theta \\ 0 & 1 & 0 \\ -\sin\theta & 0 & \cos\theta \end{bmatrix} \tag{2.9}$$

Now we need four ingredients for the linearized LL equation: $\vec{m}'_{eq}$, $\vec{H}'_{eff,eq}$, $\delta\vec{m}'$ and the deviation of effective filed $\delta\vec{H}'_{eff}$ due to $\delta\vec{m}'$. Here $\vec{m}'_{eq}$ is already known and $\delta\vec{m}'$ is the unknown variable to be solved:

$$\vec{m}'_{eq} = \begin{bmatrix} 0 \\ 0 \\ 1 \end{bmatrix} \qquad \delta\vec{m}' = \begin{bmatrix} \delta m'_x \\ \delta m'_y \\ 0 \end{bmatrix} \tag{2.10}$$

Here we assume that the deviation of the magnetization and effective field is tiny, so there are no dynamics in the z component of the magnetization. Notice that it is the lab frame magnetization components m_x and m_z that enter equation 2.2 while we only need those in the magnet frame:

$$\vec{m} = R_y(\theta)\vec{m}' = \begin{bmatrix} m'_x\cos\theta + m'_z\sin\theta \\ m'_y \\ -m'_x\sin\theta + m'_z\cos\theta \end{bmatrix} \tag{2.11}$$

Now we have the full expression for the effective field in the magnet frame:

$$\begin{aligned}\vec{H}'_{eff} &= R_y^T(\theta)\vec{H}_{eff} \\ &= \begin{bmatrix} H_0\sin(\theta_H-\theta) + m'_x(H_k\sin^2\theta - H_\perp\cos^2\theta) - m'_z(H_k+H_\perp)\sin\theta\cos\theta \\ 0 \\ H_0\cos(\theta_H-\theta) - m'_x(H_k+H_\perp)\sin\theta\cos\theta + m'_z(H_k\cos^2\theta - H_\perp\sin^2\theta) \end{bmatrix}\end{aligned} \tag{2.12}$$

Since the dynamics of $\vec{m}'$ only exist in x and y component, we can extract terms associated with m'_x and m'_y to obtain $\delta\vec{H}'_{eff}$:

$$\delta\vec{H}'_{eff} = \begin{bmatrix} \delta m'_x(H_k\sin^2\theta - H_\perp\cos^2\theta) \\ 0 \\ -\delta m'_x(H_k+H_\perp)\sin\theta\cos\theta \end{bmatrix} \tag{2.13}$$

and the remained terms are the equilibrium effective field:

$$\vec{H}'_{eff,eq} = \begin{bmatrix} H_0\sin(\theta_H-\theta) - (H_k+H_\perp)\sin\theta\cos\theta \\ 0 \\ H_0\cos(\theta_H-\theta) + H_k\cos^2\theta - H_\perp\sin^2\theta \end{bmatrix} \tag{2.14}$$

By substituting equation 2.10, 2.2, and 2.13 into 2.8, we have the eigenvalue equation:

$$\frac{d}{dt}\begin{bmatrix}\delta m'_x \\ \delta m'_y\end{bmatrix} = \begin{bmatrix} 0 & -\gamma H'_{eff,eq,z} \\ \gamma[H'_{eff,eq,z} + H_\perp\cos^2\theta - H_k\sin^2\theta] & 0 \end{bmatrix}\begin{bmatrix}\delta m'_x \\ \delta m'_y\end{bmatrix} \tag{2.15}$$

The eigenvalue of the equation 2.15 gives the FMR frequency:

$$\omega_{FMR} = \gamma\sqrt{[H_0\cos(\theta_H-\theta) + H_k\cos^2\theta - H_\perp\sin^2\theta][H_0\cos(\theta_H-\theta) + (H_k+H_\perp)\cos(2\theta)]} \tag{2.16}$$

As is mentioned previously, in the configuration in this work, $\theta = \theta_H = 0$. So the FMR frequency has a simpler form:

$$\omega_{FMR} = \gamma\sqrt{[H_0+H_k][H_0+H_k+H_\perp]} \tag{2.17}$$

FMR frequency is the natural oscillating rate of the magnet, that is, without external driving force and dissipation, how fast the magnetization oscillates. It is an inherent property of the magnet and can be modulated by H_k and $H_\perp$.

To understand the more practical magnetization dynamics, we take the dissipation into account and apply an effective oscillatory field $\vec{h}'$ due to finite temperature T (illustrated in Figure 2.5), yielding the Landau-Lifshitz-Gilbert (LLG) equation[40]:

$$\frac{d\vec{m}}{dt} = -\gamma\vec{m} \times \vec{H}_{eff} + \alpha\vec{m} \times \frac{d\vec{m}}{dt} \tag{2.18}$$

The term $\alpha\vec{m} \times \frac{d\vec{m}}{dt}$ corresponds to the dissipation which tends to rotate the magnetization back to its equilibrium. By linearization and in the magnet frame:

$$\frac{d\delta\vec{m}'}{dt} = -\gamma\vec{m}'_{eq} \times \delta\vec{H}'_{eff} - \gamma\delta\vec{m}' \times \vec{H}'_{eff,eq} - \gamma\vec{m}'_{eq} \times \delta\vec{h}' + \alpha\vec{m}'_{eq} \times \frac{d\delta\vec{m}'}{dt} \tag{2.19}$$

where α is the damping coefficient depending on the material. Since this is a stochastic equation, we would like to analyse the correlation functions of $\delta\vec{m}'$.

Here we define 2 frequency components:

$$\begin{aligned} \omega_H &= \gamma[H_0 \cos(\theta_H - \theta) + H_k \cos^2\theta - H_\perp \sin^2\theta] \\ \omega_\perp &= \gamma[H_0 \cos(\theta_H - \theta) + (H_k + H_\perp)\cos 2\theta] \end{aligned} \tag{2.20}$$

and assume that the thermal field and magnetization deviation are harmonic: $\vec{h}' \sim \mathrm{e}^{-\mathrm{i}\omega t}$ and $\delta\vec{m}' \sim \mathrm{e}^{-\mathrm{i}\omega t}$. By solving the LLG equation, we can obtain how the thermal field affects the dynamics of magnetization:

$$\begin{bmatrix} \delta m'_x \\ \delta m'_y \end{bmatrix} = \begin{bmatrix} S_{xx} & S_{xy} \\ S_{yx} & S_{yy} \end{bmatrix} \begin{bmatrix} h'_x \\ h'_y \end{bmatrix} \tag{2.21}$$

The susceptibility $S_{\mathrm{ij}}(\mathrm{i},\mathrm{j}=x,y)$ couples the j component of $\vec{h}'$ to the i component of $\delta\vec{m}'$ and can be expressed by:

$$\begin{aligned} S_{xx} &= \frac{-\gamma[\omega_H - \mathrm{i}\alpha\omega]}{\omega^2 - [\omega_H - \mathrm{i}\alpha\omega][\omega_\perp - \mathrm{i}\alpha\omega]} \\ S_{xy} &= \frac{\mathrm{i}\gamma\omega}{\omega^2 - [\omega_H - \mathrm{i}\alpha\omega][\omega_\perp - \mathrm{i}\alpha\omega]} \\ S_{yx} &= \frac{-\mathrm{i}\gamma\omega}{\omega^2 - [\omega_H - \mathrm{i}\alpha\omega][\omega_\perp - \mathrm{i}\alpha\omega]} \\ S_{yy} &= \frac{-\gamma[\omega_\perp - \mathrm{i}\alpha\omega]}{\omega^2 - [\omega_H - \mathrm{i}\alpha\omega][\omega_\perp - \mathrm{i}\alpha\omega]} \end{aligned} \tag{2.22}$$

Since $\vec{h}'$ arises from the thermal fluctuation with zero mean and local, instantaneous correlation[41][42][43]:

$$\langle h'_{\mathrm{i}}(t)h'_{\mathrm{j}}(t')\rangle = 2D_{th}\delta_{\mathrm{ij}}\delta(t-t') \qquad \Rightarrow \qquad \langle h'_{\mathrm{i}}(\omega)h'_{\mathrm{j}}(\omega)\rangle = 2\pi 2D_{th}\delta_{\mathrm{ij}}\delta(\omega+\omega) \tag{2.23}$$

where $D_{th} = \frac{\alpha k_B T}{\gamma M_s V}$ and V refers to the volume of the magnet, with the correlation functions of the thermal field and susceptibilities, we can evaluate the correlation functions of the magnetization:

$$\begin{aligned} C_{\mathrm{ij}}(t) = \langle \delta m'_{\mathrm{i}}(t)\delta m'_{\mathrm{j}}(0)\rangle &= \int \frac{d\omega}{2\pi}\int \frac{d\omega}{2\pi}\mathrm{e}^{-\mathrm{i}\omega t}\langle \delta m'_{\mathrm{i}}(\omega)\delta m'_{\mathrm{j}}(\omega)\rangle \\ &= \int \frac{d\omega}{2\pi}\int \frac{d\omega}{2\pi}\mathrm{e}^{-\mathrm{i}\omega t}2\pi 2D_{th}\delta(\omega+\omega)[S_{\mathrm{i}x}(\omega)S_{\mathrm{j}x}(-\omega) + S_{\mathrm{i}y}(\omega)S_{\mathrm{j}y}(-\omega)] \\ &= \int \frac{d\omega}{2\pi}\mathrm{e}^{-\mathrm{i}\omega t}2D_{th}[S_{\mathrm{i}x}(\omega)S_{\mathrm{j}x}(-\omega) + S_{\mathrm{i}y}(\omega)S_{\mathrm{j}y}(-\omega)] \end{aligned} \tag{2.24}$$

In frequency domain:

$$C_{\mathrm{ij}}(\omega) = 2D_{th}[S_{\mathrm{i}x}(\omega)S_{\mathrm{j}x}(-\omega) + S_{\mathrm{i}y}(\omega)S_{\mathrm{j}y}(-\omega)] \tag{2.25}$$

And each component:

$$
\begin{aligned}
C_{xx} &= 2D_{th}\gamma^2 \frac{\omega_H^2 + \omega^2(1+\alpha^2)}{[\omega^2(1+\alpha^2) - \omega_H\omega_\perp]^2 + \alpha^2\omega^2(\omega_H+\omega_\perp)^2} \\
C_{xy} &= 2D_{th}\gamma^2 \frac{-\mathrm{i}\omega(\omega_H + \omega_\perp)}{[\omega^2(1+\alpha^2) - \omega_H\omega_\perp]^2 + \alpha^2\omega^2(\omega_H+\omega_\perp)^2} \\
C_{yx} &= 2D_{th}\gamma^2 \frac{\mathrm{i}\omega(\omega_H + \omega_\perp)}{[\omega^2(1+\alpha^2) - \omega_H\omega_\perp]^2 + \alpha^2\omega^2(\omega_H+\omega_\perp)^2} \\
C_{yy} &= 2D_{th}\gamma^2 \frac{\omega_\perp^2 + \omega^2(1+\alpha^2)}{[\omega^2(1+\alpha^2) - \omega_H\omega_\perp]^2 + \alpha^2\omega^2(\omega_H+\omega_\perp)^2}
\end{aligned}
\tag{2.26}
$$

The correlation functions in frequency domain $C_{\mathrm{ij}}(\omega)$ cover the information of the magnetization dynamics and composite the power spectrum of the fluctuating magnetic field felt by the NV center (stray field). Before talking about the NV center, we need to investigate how the magnetization is related to the stray field.

2.2 Stray field

In this work, the magnet is a uniformly magnetized cuboid with size (L_x, L_y, L_z). We want to study how each component of the magnetization contributes to the magnetic field at the point $\vec{r} = (x, y, z)$. We can first consider the z component, and the contribution from other components can be obtained by a cyclical shift in $\{x, y, z\}$ and $\{L_x, L_y, L_z\}$. In this section, we use the lab frame, and the prime ($\prime$) denotes the internal region of the cuboid.

Each instance the magnetization deviation $\delta\vec{m}$ reaches its new state, there will be a transient response of the electromagnetic (EM) filed[40]. If the establishment of the new steady EM field is much faster than the magnetization dynamics, the EM field can be considered instantaneously evolving with the magnetization[40]. In this work, the time scale of EM transient response ($Ly/c \sim 10^{-15}s$) is much less than that of magnetization dynamics ($1/\omega \sim 10^{-9}s$), so the magnetostatics approximation is valid and takes the form[44][45]:

$$
\vec{\nabla} \cdot \vec{B} = 0 \qquad \vec{\nabla} \times \vec{H} = 0 \tag{2.27}
$$

The material equation tells us:

$$\vec{B} = \vec{H} + 4\pi\vec{M} \tag{2.28}$$

By defining a scalar potential Φ, we can obtain the magnetic field by:

$$\vec{H} = -\vec{\nabla}\Phi \tag{2.29}$$

Equation 2.27, 2.28 and 2.29 imply the Poisson equation:

$$\vec{\nabla}^2\Phi = 4\pi\vec{\nabla}\cdot\vec{M} \tag{2.30}$$

and we already know the Green's function solution to the Poisson function:

$$\vec{\nabla}^2 G(\vec{r}-\vec{r'}) = \delta(\vec{r}-\vec{r'}) \qquad \Rightarrow \qquad G(\vec{r}-\vec{r'}) = -\frac{1}{4\pi\left|\vec{r}-\vec{r'}\right|} \tag{2.31}$$

Here $\vec{r'}$ is the point inside the magnet. Green's function can be considered as the unit impulse response of the Poisson equation. Hence, the scalar potential can be evaluated by:

$$\Phi(\vec{r}) = \int_V d\vec{r'} G(\vec{r}-\vec{r'}) 4\pi\vec{\nabla}'\cdot\vec{M}(\vec{r'}) = \int_V d\vec{r'} \frac{\vec{\nabla}'\cdot\vec{M}(\vec{r'})}{\left|\vec{r}-\vec{r'}\right|} \tag{2.32}$$

where V denotes the entire space inside the magnet. In our case, the magnetization is uniformly along the z-axis, so the divergence of the magnetization is zero except for the top and bottom surfaces of z direction, where $\vec{\nabla}'\cdot\vec{M}(\vec{r'})$ can be evaluated by:

$$\vec{\nabla}'\cdot\vec{M}(\vec{r'}) = M_s(\delta(z'-L_z) - \delta(z'-0)) \tag{2.33}$$

As is shown in Figure 2.6, we can consider this as the magnetic "charges" with density M_s distributed on the top and bottom of the magnet. So the scalar potential can be reduced to:

$$\Phi(\vec{r}) = -M_s \int_0^{L_x} dx' \int_0^{L_y} dy' \left(\frac{1}{|\vec{r}-(x',y',L_z)|} - \frac{1}{|\vec{r}-(x',y',0)|} \right) \tag{2.34}$$

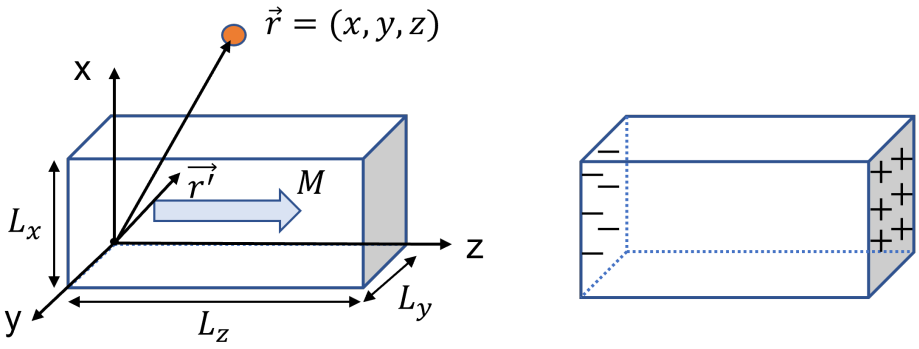

Figure 2.6. Geometry of the magnet and the effective "charges"

By taking the gradient of the scalar potential we have the stray field generated by the z component of the magnetization[44][45]:

$$\vec{H}^z(\vec{r}) = M_s \int_0^{L_x} dx' \int_0^{L_y} dy' \left(\frac{\vec{r} - (x', y', L_z)}{|\vec{r} - (x', y', L_z)|^3} - \frac{\vec{r} - (x', y', 0)}{|\vec{r} - (x', y', 0)|^3} \right) \tag{2.35}$$

Equation 2.35 can by analytically integrated and each component of the stray field is[46]:

$$\begin{aligned}
B_x^z(x, y, z, L_x, L_y, L_z) &= M_s\{f(x, y, z) - f(x, y - L_y, z) \\
&\quad - f(x - L_x, y, z) + f(x - L_x, y - L_y, z)\} \\
B_y^z(x, y, z, L_x, L_y, L_z) &= M_s\{f(y, x, z) - f(y - L_y, x, z) \\
&\quad - f(y, x - L_x, z) + f(y - L_y, x - L_x, z)\} \\
B_z^z(x, y, z, L_x, L_y, L_z) &= M_s\{g(x, y, L_z, z) - g(x, y - L_y, L_z, z) \\
&\quad - g(x - L_x, y, L_z, z) + g(x - L_x, y - L_y, L_z, z) \\
&\quad - g(x, y, 0, z) + g(x, y - L_y, 0, z) \\
&\quad + g(x - L_x, y, 0, z) - g(x - L_x, y - L_y, 0, z)\}
\end{aligned} \tag{2.36}$$

where:

$$f(a,b,c) = \log\left(\frac{\sqrt{a^2+(c-L_c)^2}(b+\sqrt{a^2+b^2+c^2})}{\sqrt{a^2+c^2}(b+\sqrt{a^2+b^2+(c-L_c)^2})}\right)$$
$$g(a,b,c,d) = \arctan\left(\frac{ab}{(d-c)\sqrt{a^2+b^2+(d-c)^2}}\right) \tag{2.37}$$

Other $B_{\mathrm{i}}^{\mathrm{j}}$ can be obtained by cyclically shifting x, y, z and L_x, Ly, L_z. For example:

$$B_z^y(x,y,z,L_x,L_y,L_z) = B_x^z(z,x,y,L_z,L_x,L_y)$$

$B_{\mathrm{i}}^{\mathrm{j}}$ describes how the j component of the magnetization contributes to the i component of magnetic field at the position $\vec{r}$. We can express this in matrix form:

$$\begin{bmatrix} H_{stray,x} \\ H_{stray,y} \\ H_{stray,z} \end{bmatrix} = \begin{bmatrix} B_x^x & B_x^y & B_x^z \\ B_y^x & B_y^y & B_y^z \\ B_z^x & B_z^y & B_z^z \end{bmatrix} \begin{bmatrix} \delta m_x \\ \delta m_y \\ \delta m_z \end{bmatrix} \tag{2.38}$$

where $H_{stray,\mathrm{i}}$ denotes the i component of the stray field at the NV center in the lab frame. To apply equation 2.38 to other frame, some rotation operators may need to act on the B matrix. For example, to obtain the relation between the stray field in the lab frame $\vec{H}_{stray}$ and the magnetization deviation in the magnet frame $\delta\vec{m}'$, the transformation $\bar{B} = BR_y(\theta)$ enables the use of 2.38 by $\vec{H}_{stray} = \bar{B}\delta\vec{m}' = BR_y(\theta)\delta\vec{m}' = B\delta\vec{m}$. Notice that the equilibrium of the magnetization is along the z-axis. When the NV center is placed above the center of the zy surface of the magnet $\vec{r} = (h_{NV}, L_y/2, L_z/2)$, the equilibrium of the stray field at the NV center is also along the z-axis. Meanwhile the deviation of the magnetization $\delta\vec{m}$ generates the fluctuating x and y components of the stray field. Given the external field $\vec{H}_0$ along the z-axis, the net stray field is:

$$H_x = H_{stray,x} \qquad H_y = H_{stray,y} \qquad H_z = H_0 + H_{stray,z} \tag{2.39}$$

Now we have the information of the magnetization dynamics and how they couple to the magnetic field at the NV center. In the following section, we shall discuss the NV center itself and how such a stray field affects its dynamics.

2.3 The NV center

The NV center is a point defect in diamond - a nitrogen atom replaces a carbon atom, and a vacancy substitutes the carbon atom adjacent to the nitrogen. The crystalline structure is shown in Figure 2.7.

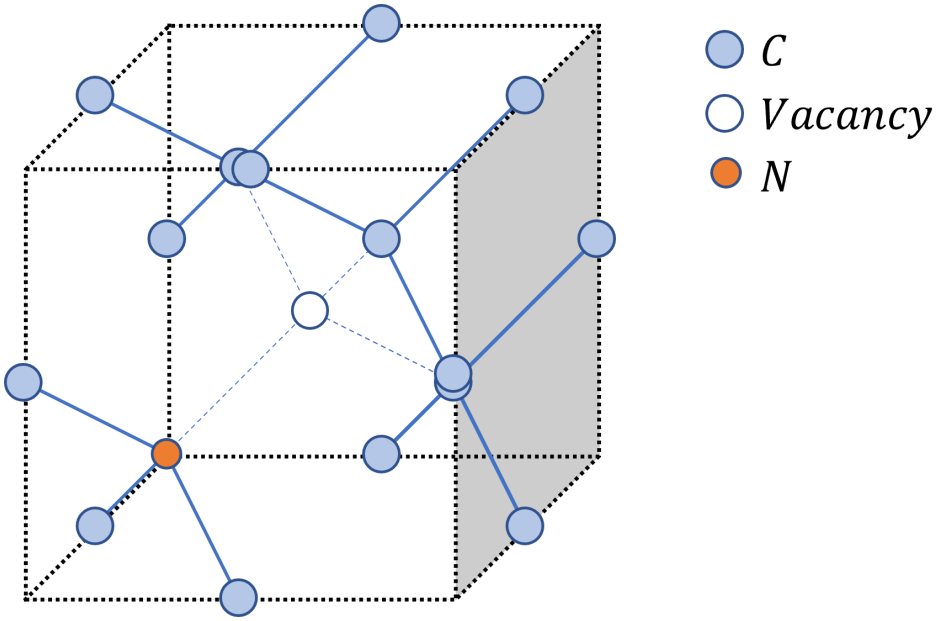

Figure 2.7. Crystalline structure of an NV center in diamond

The NV axis is along [111] direction (for simplicity, hereafter we will align the NV axis to the z-axis) and has C_{3v} symmetry (After rotation about the NV axis for $2\pi/3$, the atoms overlap with the previous structure). Depending on the number of electrons involved in the NV defect, there are three kinds of NV centers: positively charged NV^+, neutral NV^0, and negatively charged NV^-. Since only NV^- is magneto-optically active, in this work, we will focus on the NV^-, and all the NV refers to NV^- [24]. As is shown in Figure 2.9, six electrons are involved in the electronic state of the NV center - each carbon near the vacancy

provides one electron and the nitrogen gives two electrons (these five electrons are also called dangling bonds), the sixth electron is captured from the lattice[24][47].

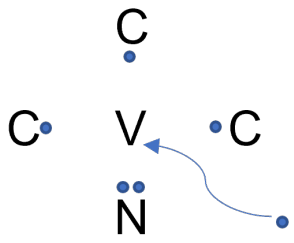

Figure 2.8. Flat structure of the NV center

The configuration of the six electrons can be described by 4 orbital states (a linear combination of the atom orbital states) $a_1', a_1, \mathrm{e}_x, \mathrm{e}_y$ whose view along [111] direction is shown as below (adapted from [48]): The most symmetry orbitals a_1' and a_1 have the lowest

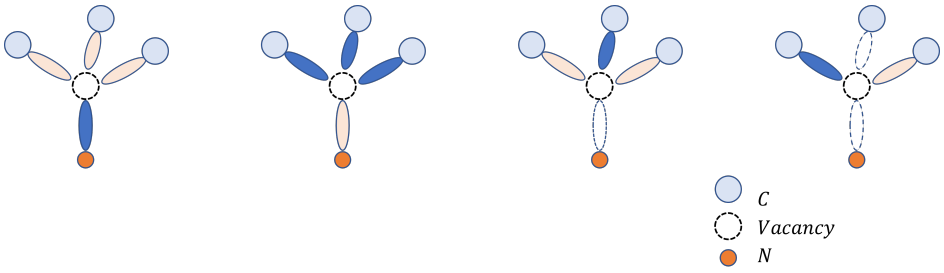

Figure 2.9. The orbital states of the NV center. The colors represent the sign of each orbital.

energy and are fulfilled in the ground state. The rest two electrons can be distributed on e_x and e_y orbitals. By Hund's first rule, the ground state configuration prefers to maximize the total spin quantum number S, which is consistent with the Pauli exclusion principle[49]. The antisymmetric scheme of orbital combination minimizes the Coulomb energy, so each electron occupies either e_x or e_y orbital, leading to a ground state triplet[48]. The configuration of electrons in the ground state is shown in Figure 2.10, where the dashed arrows indicate that we can view this six-electron system as two holes with $S = 1$. Now we have the orbital configuration of the electrons, and following we are going to discuss the spin-related properties of the NV center.

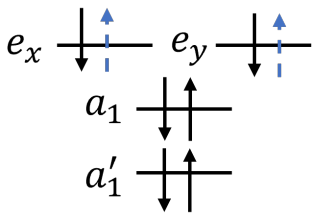

Figure 2.10. Configuration of electrons in ground state

2.3.1 Energy levels, optical readout and initialization of the NV center

The energy levels of the NV center is shown in Figure 2.11:

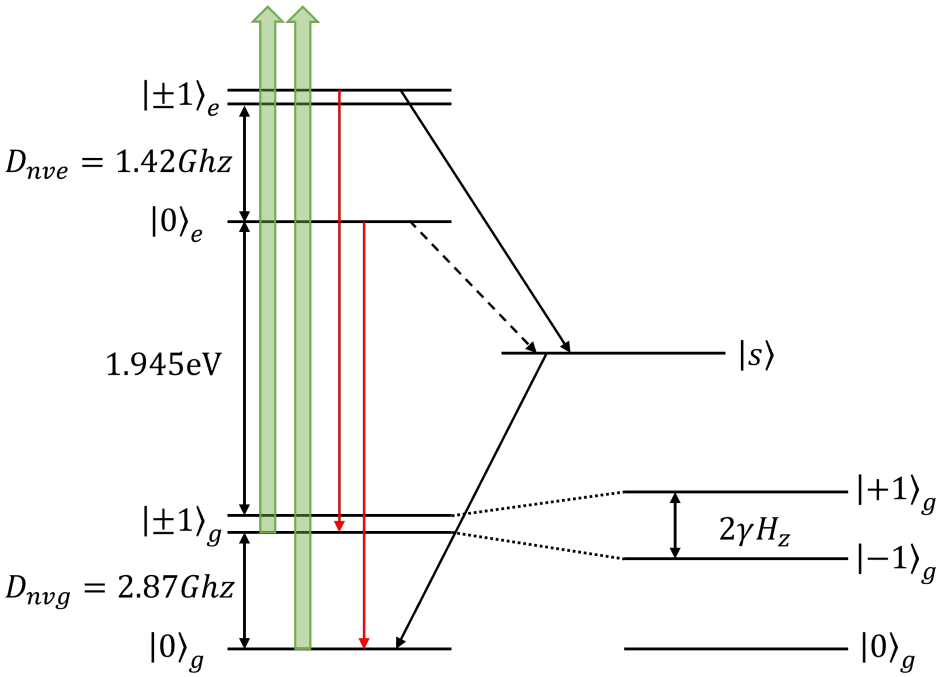

Figure 2.11. Energy level diagram of the NV center, Zeeman effect taken into account

The ground state triplet is denoted by $|0\rangle_g$, $|+1\rangle_g$ and $|-1\rangle_g$ with $m_s = 0$, $m_s = +1$ and $m_s = -1$. Similarly the excited state triplet is represented by $|0\rangle_e$, $|+1\rangle_e$ and $|-1\rangle_e$. Coulomb interaction introduced the gap of 1.945eV between the ground state triplet and the excited state triplet[48]. For the ground state the spin-spin interaction leads to the zero-field-splitting (ZFS) $D_{nvg} = 2.87GHz$[48]. Due to the axial symmetry of the NV center, the $|\pm1\rangle$ states are degenerate[24]. The magnetic field along z-axis splits the ground states $|+1\rangle_g$

and $|-1\rangle_g$. The metastable singlet state is denoted by $|s\rangle$. Since we are not going through its properties in detail, in this work we simplify the metastable singlet manifold into a single level.

One advantage of the NV center is the convenient room-temperature optical initialization and readout[15]. Typically the ground-state spins of the NV center are pumped by a $532nm$ green laser while the spins in excited states can undergo radiative and irradiative ways back to the ground states[50]. Notice that the radiative pumping and decaying are strongly spin preserving. For example, if the $m_s = 0$ state is pumped to its excited state or decays with photoluminescence, it is still $m_s = 0$[24]. The non-optical decaying is via the metastable state and the irradiative rate of $m_s = \pm 1$ is about 10 times of $m_s = 0$[51][52][53]. As is shown in Figure 2.12, within finite cycles, there will be a difference in the photoluminescence intensity of $m_s = 0$ and $m_s = \pm 1$. Such spin-dependent transient contrast facilitates the optical readout of the NV center. Meanwhile, the $|s\rangle$ state finally decays to the $|0\rangle_g$ state. After sufficiently long time, about 80% of population is in $m_s = 0$ state and we can consider the system is initialized to $|0\rangle_g$.

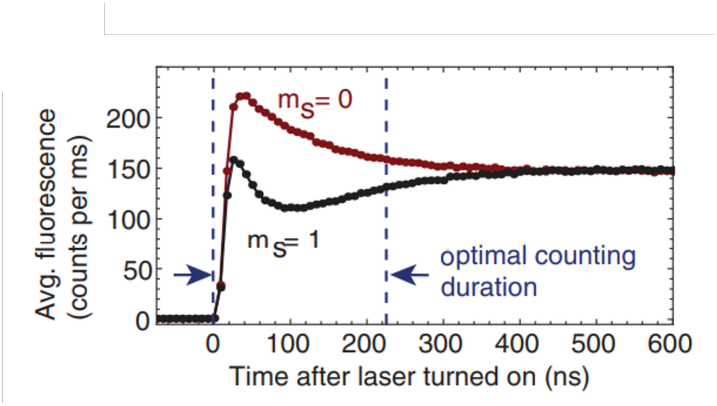

Figure 2.12. Transient response of fluorescence intensity of $m_s = 0$ and $m = 1$ state, the integration of the difference between two curves gives the practical readout results. [Reprinted/Adapted] with permission from [54] © The Optical Society.

Now we have the spin and optical properties of the NV center. Following, we will go through the Hamiltonian describing the interaction with magnetic and electric fields. Then we will try to extract the effective two-level system for further calculation.

2.3.2 Hamiltonian of the NV center and the effective two-level system

To investigate how the NV center states evolve under external perturbation, we may need the Hamiltonian of the ground state NV center[55][56][34]:

$$\mathcal{H} = (D_{nvg} + \chi_{\parallel} E_z)(S_z^2 - \frac{1}{3}S(S+1)) + \gamma \vec{H} \cdot \vec{S} - \chi_{\perp}[E_x(S_x S_y + S_y S_x) + E_y(S_x^2 - S_y^2)] \quad (2.40)$$

Here the NV center crystalline axis is aligned to the z-axis and the Hamiltonian is defined by letting $\hbar = 1$. The D_{nvg} features the zero field splitting, with eigenstates $|0\rangle_g$, $|+1\rangle_g$ and $|-1\rangle_g$. The second term $\gamma \vec{H} \cdot \vec{S}$ describes the interaction with the magnetic field, where $\vec{S} = [S_x, S_y, S_z]$ is a vector spin operator consisting of corresponding Pauli matrices $S_{\mathrm{i}}, \mathrm{i} = \{x, y, z\}$. Figure 2.13 illustrates such interaction (Zeeman effect): When a magnetic field is applied, the z component H_z splits the energy levels $|+1\rangle_g$ and the $|-1\rangle_g$ by γH_z[24]; Meanwhile, the transverse component $H_{x,y}$ causes the transition between $|0\rangle_g$ and $|\pm 1\rangle_g$. If the transverse magnetic field is noisy, such incoherent transition will result in the population relaxation whose transition rate is related to the power spectrum of the the magnetic noise.

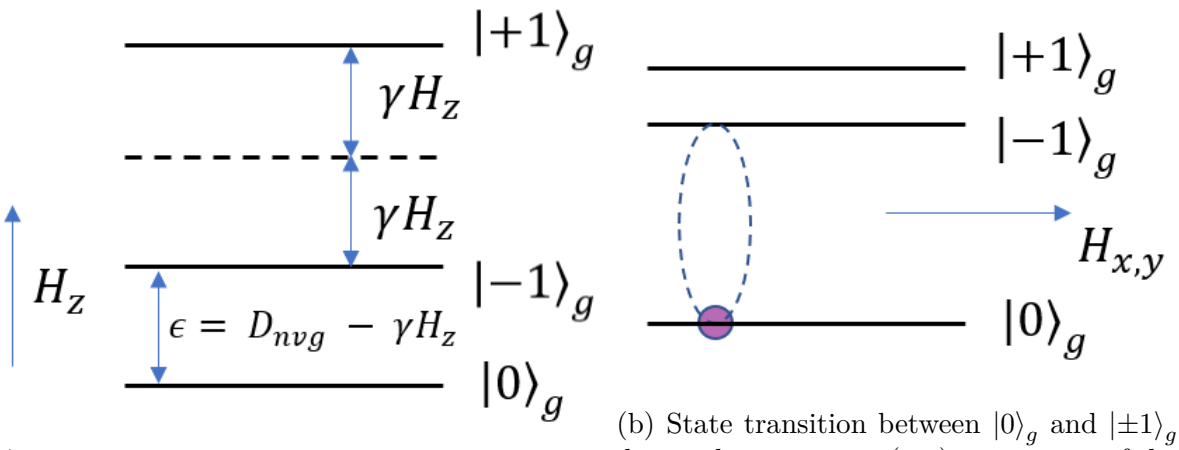

(a) Energy splitting of the NV ground triplet due to the z component of the magnetic field

(b) State transition between $|0\rangle_g$ and $|\pm 1\rangle_g$ due to the transverse (x,y) component of the magnetic field

Figure 2.13. Zeeman effect on the NV ground state triplet

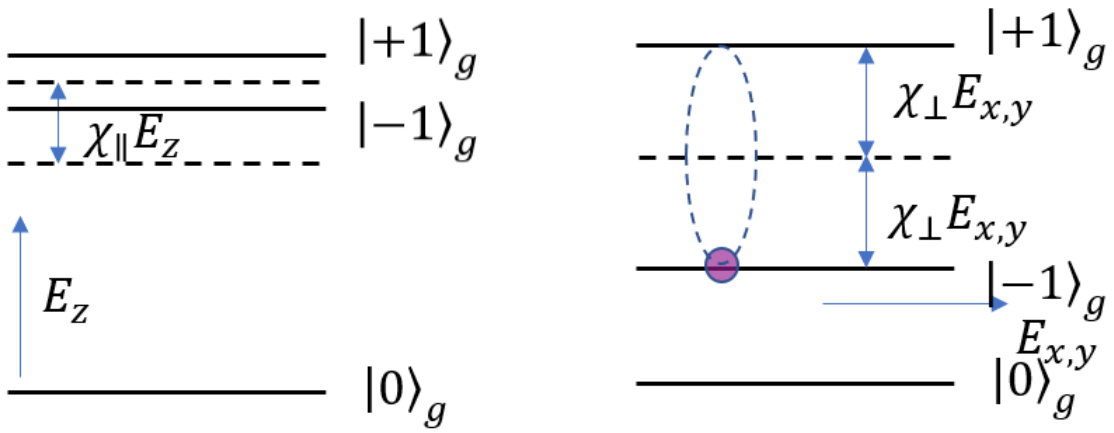

(a) Energy lifting of the $|\pm1\rangle_g$ due to the z component of the electric field

(b) Splitting between $|-1\rangle_g$ and $|+1\rangle_g$ and their mutual transition due to the transverse (x,y) component of the electric field

Figure 2.14. Stark effect on the NV ground state triplet

As is shown in Figure 2.14, the z component of the electric field induces further splitting between $|0\rangle_g$ and $|\pm1\rangle_g$ by $\chi_{\parallel}E_z$ while the transverse component $E_{x,y}$ splits between $|+1\rangle_g$ and $|-1\rangle_g$ and may cause the transition between them. In this Hamiltonian, we would like to point out that the coupling strengths to the electric field $\chi_{\parallel} = 0.35Hz/(V/cm)$, $\chi_{\perp} = 17Hz/(V/cm)$ are much lower than the magnetic field $\gamma = 2.8MHz/G$. Such facts constitute the motivation of this work to convert the electric field into magnetic noise to take advantage of the stronger magnetic coupling for sensitivity enhancement. In this work, we will not couple the NV center directly to the electric field, so we can simplify the Hamiltonian by omitting the electric field terms and choosing another energy reference:

$$\mathcal{H} = D_{nvg}S_z^2 + \gamma\vec{H}\cdot\vec{S} = \begin{bmatrix} D_{nvg}+\gamma H_z & \frac{\gamma}{\sqrt{2}}[H_x - \mathrm{i}H_y] & 0 \\ \frac{\gamma}{\sqrt{2}}[H_x + \mathrm{i}H_y] & 0 & \frac{\gamma}{\sqrt{2}}[H_x - \mathrm{i}H_y] \\ 0 & \frac{\gamma}{\sqrt{2}}[H_x + \mathrm{i}H_y] & D_{nvg}-\gamma H_z \end{bmatrix} \tag{2.41}$$

With appropriate magnetic field applied, the transition between $|0\rangle_g$ and $|-1\rangle_g$ state dominates (In [57], when $H = 200G$, the transition almost only exists between $|0\rangle_g$ and $|-1\rangle_g$). In that case, we can only consider $|0\rangle_g$ and $|-1\rangle_g$ states, extracting them as the effective two-

level system. Correspondingly the lower right four terms in the full Hamiltonian constitute the Hamiltonian of the effective two-level system:

$$\mathcal{H}(t) = \begin{bmatrix} 0 & \frac{\gamma}{\sqrt{2}}[H_x - \mathrm{i}H_y] \\ \frac{\gamma}{\sqrt{2}}[H_x + \mathrm{i}H_y] & D_{nvg} - \gamma H_z \end{bmatrix} \tag{2.42}$$

In section 2.2, we find that there is no dynamics in H_z while the fluctuation exists in H_x and H_y. Hence the effective Hamiltonian can be divided into a time-invariant Hamiltonian and the perturbation Hamiltonian:

$$\mathcal{H}(t) = \mathcal{H}_0 + V(t) = \begin{bmatrix} 0 & 0 \\ 0 & D_{nvg} - \gamma H_z \end{bmatrix} + \begin{bmatrix} 0 & \frac{\gamma}{\sqrt{2}}[H_x - \mathrm{i}H_y] \\ \frac{\gamma}{\sqrt{2}}[H_x + \mathrm{i}H_y] & 0 \end{bmatrix} \tag{2.43}$$

Now we have the effective two-level system model for the NV ground states. With the effective Hamiltonian, we can study the dynamics of the NV ground states.

2.3.3 Dynamics of the NV center - population relaxation

As is shown in equation 2.43, appearing at the off-diagonal elements in perturbation Hamiltonian $V(t)$, the noisy transverse magnetic field can cause the random transition between $|0\rangle_g$ and $|-1\rangle_g$, leading to the population relaxation. To estimate the transition rate Γ, we begin with the time evolution of the ground states, which is described by the Schrodinger equation[58]:

$$\mathrm{i}\frac{d}{dt}|\psi(t)\rangle = [\mathcal{H}_0 + V(t)]\,|\psi(t)\rangle \tag{2.44}$$

Since the evolution due to time-independent Hamiltonian $\mathcal{H}_0$ is easy to solve ($U_{\mathcal{H}_0}(t) = \mathrm{e}^{-\mathrm{i}\mathcal{H}_0 t}$), we can remove the time dependence of the state vector due to $\mathcal{H}_0$ by applying the conjugate time evolution operator related to it:

$$|\psi(t)\rangle_I = \mathrm{e}^{\mathrm{i}\mathcal{H}_0 t}\,|\psi(t)\rangle \tag{2.45}$$

When writing the Schrodinger equation for $|\psi(t)\rangle_I$, we find that the Hamiltonian $\mathcal{H}_0$ is canceled while the Heisenberg version of the perturbation $V(t)$ remains:

$$V(t)_I = \mathrm{e}^{\mathrm{i}\mathcal{H}_0 t} V(t) \mathrm{e}^{-\mathrm{i}\mathcal{H}_0 t} \tag{2.46}$$

Such version of state vector and perturbation Hamiltonian constitute the interaction picture, where the Schrodinger equation reads:

$$\mathrm{i}\frac{d}{dt}|\psi(t)\rangle_I = V_I(t)\,|\psi(t)\rangle_I \tag{2.47}$$

In the interaction picture, we can focus on the perturbation Hamiltonian because we already take the time-independent Hamiltonian into account by the transformation in equation 2.45 and 2.46. The first order solution to 2.47 equation is:

$$|\psi(t)\rangle_I = |\psi(0)\rangle_I - \mathrm{i}\int_0^t dt V_I(t)\,|\psi(t)\rangle_I \tag{2.48}$$

When the perturbation is very weak, we can ignore the higher order integration and hence:

$$|\psi(t)\rangle_I \approx |\psi(0)\rangle_I - \mathrm{i}\int_0^t dt V_I(t)\,|\psi(0)\rangle_I \tag{2.49}$$

Since the NV center is initialized to $|0\rangle_g$, $|\psi(0)\rangle_I = |0\rangle_g$. The probability of the state $|\psi(t)\rangle_I$ in $|-1\rangle_g$ indicates the transition probability for a unit population and is given by the absolute square of its projection on $|-1\rangle_g$:

$$P_{0\to-1} = \langle|_g\langle -1| - \mathrm{i}\int_0^t dt V_I(t)|0\rangle_g|^2\rangle_f \tag{2.50}$$

where $\langle\rangle_f$ denotes averaging over many realizations of the noise. By substitution of the perturbation Hamiltonian we have:

$$\begin{aligned} P_{0\to-1} &= \langle|\int_0^t dt \frac{\gamma}{\sqrt{2}}(H_x(t) + \mathrm{i}H_y(t))\mathrm{e}^{\mathrm{i}\epsilon t}|^2\rangle_f \\ &= \frac{\gamma^2}{2}\int_0^t dt_1 \int_0^t dt_2 \mathrm{e}^{\mathrm{i}\epsilon(t_1-t_2)}\langle(H_x(t_1) + \mathrm{i}H_y(t_1))(H_x(t_2) - \mathrm{i}H_y(t_2))\rangle_f \end{aligned} \tag{2.51}$$

where $\epsilon = D_{nvg} - \gamma H_z$ is the energy gap between $|0\rangle_g$ and $|-1\rangle_g$. This equation implies the need for evaluation of the correlation functions of magnetic field at the NV center. Fortunately, equation 2.38 gives the relation between the stray field H_i and the magnetization deviation $\delta m'_\mathrm{i}$ and we already know the correlation functions of $\delta m'_\mathrm{i}$ by equation 2.24 and 2.26. By substitution, we have:

$$\begin{aligned} P_{0\to-1} = \frac{\gamma^2}{2}\int_0^t dt_1 \int_0^t dt_2 \mathrm{e}^{\mathrm{i}\epsilon(t_1-t_2)}[&(\bar{B}_x^{x2} + \bar{B}_y^{x2})\langle \delta m'_x(t_1)\delta m'_x(t_2)\rangle_f \\ &+ \mathrm{i}(\bar{B}_y^y \bar{B}_x^x - \bar{B}_x^y \bar{B}_y^x)\langle \delta m'_y(t_1)\delta m'_x(t_2)\rangle_f \\ &- \mathrm{i}(\bar{B}_y^y \bar{B}_x^x - \bar{B}_x^y \bar{B}_y^x)\langle m'_x(t_1)\delta m'_y(t_2)\rangle_f + (\bar{B}_x^{y2} + \bar{B}_y^{y2})\langle m'_y(t_1)\delta m'_y(t_2)\rangle_f] \\ = \int_{-\infty}^{\infty} \frac{d\omega}{2\pi} \tilde{K}(\omega) &\left(\frac{\sin\left(\frac{\omega-\epsilon}{2}t\right)}{\frac{\omega-\epsilon}{2}}\right)^2 \end{aligned} \tag{2.52}$$

where $\tilde{K}(\omega)$ denotes the power spectral density of the perturbation field $\frac{\gamma}{2}[H_x + \mathrm{i}H_y]$ and is evaluated by:

$$\begin{aligned} \tilde{K}(\omega) = \frac{\gamma^2}{2}[&(\bar{B}_x^{x2} + \bar{B}_y^{x2})C_{xx} + \mathrm{i}(\bar{B}_y^y \bar{B}_x^x - \bar{B}_x^y \bar{B}_y^x)C_{yx} \\ &- \mathrm{i}(\bar{B}_y^y \bar{B}_x^x - \bar{B}_x^y \bar{B}_y^x)C_{xy} + (\bar{B}_x^{y2} + \bar{B}_y^{y2})C_{yy}] \end{aligned} \tag{2.53}$$

The sinc-like function $\left(\frac{\sin\left(\frac{\omega-\epsilon}{2}t\right)}{\frac{\omega-\epsilon}{2}}\right)^2$ has a peak at $\omega = \epsilon$ and the first lobe is in $I = [\epsilon - \pi/t, \epsilon + \pi/t]$, which contributes most of the integration. When the interrogation time t is long enough, the interval I is narrow enough such that the sinc-like function can be approximated by a δ function, which is illustrated by Figure 2.15 using the typical parameters of simulations in this work ($\epsilon = 1GHz, t = 10\mu s$). In this case, the transition probability can be evaluated by:

$$P_{0\to-1} = \tilde{K}(\omega = \epsilon)t \tag{2.54}$$

The transition rate is defined by the time derivative of the transition probability, therefore:

$$\Gamma = \tilde{K}(\omega = \epsilon) \tag{2.55}$$

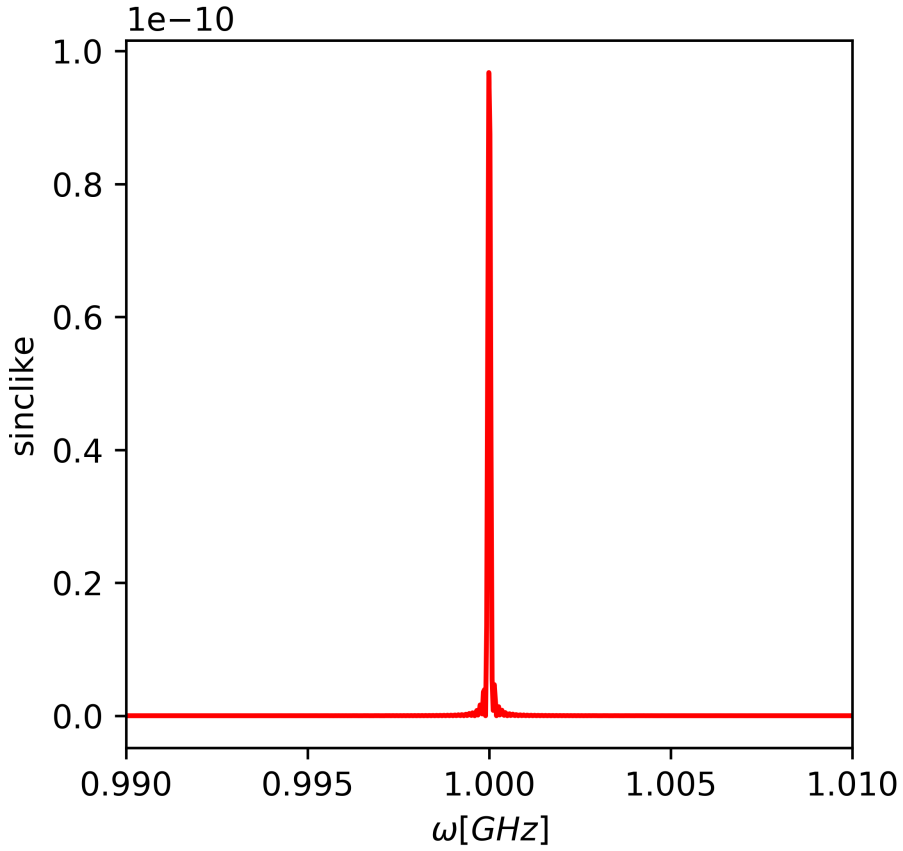

Figure 2.15. Sinc-like function with the typical parameters used in this work, the first lobe is narrow enough to approximate it by a δ function

One can also try to figure out the transition rate for $|-1\rangle_g \rightarrow |0\rangle_g$ transition and will find it the same as 2.55. Transition rate tells us the transition probability in unit time for unit population. For practical population dynamics illustrated in Figure 2.16, we need to solve:

$$\begin{aligned} \frac{d}{dt}p_0 &= -\Gamma(p_0 - p_{-1}) \\ \frac{d}{dt}p_{-1} &= \Gamma(p_0 - p_{-1}) \end{aligned} \tag{2.56}$$

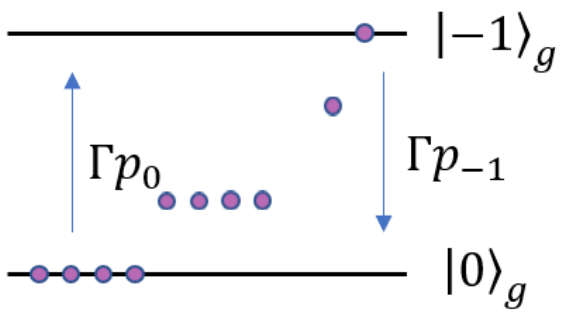

Figure 2.16. Population transition between $|0\rangle_g$ and $|-1\rangle_g$, with the same mutual transition rate, more population means more transition in unit time

where p_0 and p_{-1} denote the population of $|0\rangle_g$ and $|-1\rangle_g$. Since we initialize the NV cneter in $|0\rangle_g$:

$$\begin{aligned} p_0(t=0) &= 1 \\ p_{-1}(t=0) &= 0 \end{aligned} \tag{2.57}$$

We can find that the population relaxation is exponential:

$$\begin{aligned} p_0(t) &= \frac{1}{2}(1+\mathrm{e}^{-2\Gamma t}) \\ p_{-1}(t) &= \frac{1}{2}(1-\mathrm{e}^{-2\Gamma t}) \end{aligned} \tag{2.58}$$

Now we have the full story of how the magnetization dynamics arising from the finite temperature result in the population relaxation of the NV center. As for electric field sensing, we need to figure out how the electric field applied modulates the parameters and finally give rise to the quantity we measure - the population difference δp.

2.4 Electric-field-induced population difference

The first parameter modulated by the electric field is the magnetic anisotropy (H_k or $H_\perp$) of the sample. This work will focus on VCMA and compare the results with another

way of modulation - electric-field-induced magnetoelastic effect using PMN-PT (Hereafter, we will call it PMN-PT for simplification).

VCMA (voltage-controlled magnetic anisotropy) effect exists at the interface between a ferromagnetic metal and a dielectric material [59]. Many mechanisms of VCMA can be explained by the second-order correction energy by spin-orbit coupling (SOC)[60]:

$$E_{ani} = E_{SOC}(z) - E_{SOC}(x) = \upsilon^2 \sum_{o,u} \frac{|\langle o|L_z|u\rangle|^2 - |\langle o|L_x|u\rangle|^2}{E_u - E_o} \tag{2.59}$$

where υ is the SOC strength, $|o\rangle$ and $|u\rangle$ denote the occupied and unoccupied orbital states, E_o and E_u are the eigen energy of the corresponding occupied and unoccupied states. Such expression depicts the SOC-induced energy difference between the two magnetization orientations, i.e., magnetic anisotropy energy.

When exposed to an electric field, the conduction electrons are redistributed on the surface of the metal to cancel the electric field in bulk. However, such charge accumulation/depletion is highly spin-selective in ferromagnetic materials due to exchange interaction, causing surface magnetization [61]. In [62], the electric-field-induced magnetocrystalline anisotropy is discussed with experiment results, where the change of charge density at different d orbitals shifts the coupling between the occupied and unoccupied orbital states via the L_x and L_z operators, which relates to the numerator in equation 2.59. The change in the band structure can also account for the VCMA - the band lowering or lifting may directly modify the denominator of equation 2.59 and in turn affect the filling level of the orbital, rendering the variation of the numerator in equation 2.59. In [63], the coupling between the p orbital and the d orbital leads to the splitting of the two bands. In [64] the strain also introduces the band structure shifting.

Experimentally, VCMA tunes the interfacial anisotropy by [59]:

$$\frac{K_{\mathrm{i}}(E)}{L_x} = \frac{K_{\mathrm{i}}(0) - \beta E}{L_x} \tag{2.60}$$

where $K_{\mathrm{i}}(0)$ and $K_{\mathrm{i}}(E)$ are the interfacial anisotropy without and with the electric field, respectively, β is the VCMA coefficient, and L_x denotes the effective thickness of the ferromag-

net. In [59], the effective magnetic anisotropy energy has the phenomenological expression:

$$K_{eff} = \left(K_V - 2\pi M_s^2\right) + \frac{K_{\mathrm{i}}}{L_x} \tag{2.61}$$

where K_V is the volume anisotropy, and M_s is the saturation magnetization. Notice that here K_{eff} is the anisotropy energy in the out-of-plane direction (the x-axis), so it corresponds to the term $H_\perp$ term in equation 2.1. Hence, according to 2.2, we can have the effective $H_\perp$:

$$H_\perp = 4\pi M_s - \frac{2K_V}{M_s} - \frac{2K_{\mathrm{i}}(0)}{M_s L_x} + \frac{2\beta}{M_s L_x} E \tag{2.62}$$

For simplicity, we define:

$$\xi_{VCMA} = \frac{dH_\perp}{dE} = \frac{2\beta}{M_s L_x} \tag{2.63}$$

to denote how much the $H_\perp$ changes with the electric field.

The electric-field-induced magnetoelastic effect using PMN-PT utilizes the inverse version of the strain/stress-mediated magnetoelectric (ME) effect - the piezoelectric material converts the electric field into the strain, which is applied to the magnetic material and changes its magnetic anisotropy[65]:

$$H_k = \frac{3\lambda_s Y d_{eff}}{M_s} E \tag{2.64}$$

where λ_s is the saturation magnetostriction, d_{eff} is the effective piezomagnetic coefficient, Y is the Young's Modulus of the magnet. Similarly, we define:

$$\xi_{PMN-PT} = \frac{dH_k}{dE} = \frac{3\lambda_s Y d_{eff}}{M_s} \tag{2.65}$$

to denote the rate of H_k change due to the electric field. The free energy of the PMN-PT has the form[66]:

$$\mathcal{F} = -M_s \vec{m} \cdot \vec{H}_0 - H_k' \frac{M_s}{2}(m_z^2 - m_y^2) + \frac{M_s}{2} H_\perp' m_x^2 \tag{2.66}$$

Since $m_x^2 + m_y^2 + m_z^2 = 1$, by transformation: $H_k = 2H_k'$ and $H_\perp = H_\perp' - H_k'$, we can still obtain the previous effective field equation 2.2 and hence the FMR frequency equation 2.1.2 applies to PMN-PT case.

Now we know that how the electric field tunes the magnetic anisotropy, then by equation 2.24, the correlation functions of δm_{i} are modulated by the anisotropy and enter the $\tilde{K}(\omega)$ by equation 2.53 so that the transition rate Γ in equation 2.55 is changed. However, another way of propagation would be simpler under some assumption: if the electric field is tiny such that the shape of $\tilde{K}(\omega)$ is almost not changed but only shifted by $\Delta\omega_{FMR}$, then we can think that the electric field effectively modulates the FMR frequency, shifts the $\tilde{K}(\omega)$, and finally results in the $\Delta\Gamma$, which is qualitatively shown in Figure 2.17

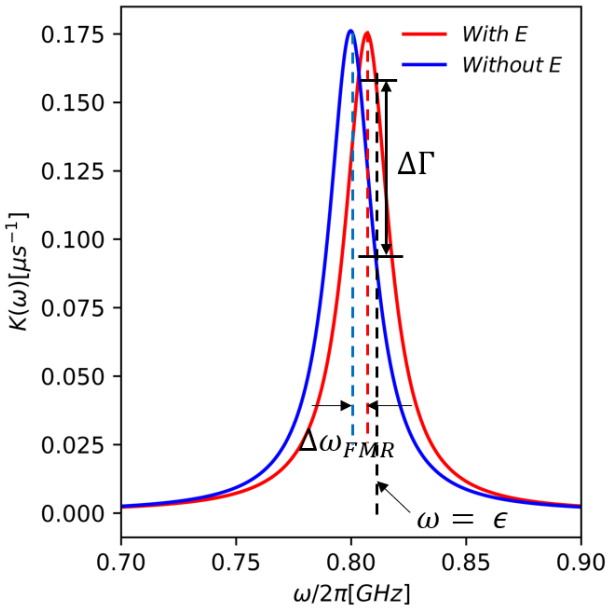

Figure 2.17. Shift of $\tilde{K}(\omega)$ and the induced $\Delta\Gamma$

The overall modulation of Γ can be denoted by a function of E and we take the first order Taylor expansion:

$$\Gamma(E) = \Gamma(E_0) + \frac{d\Gamma}{dE}|_{E=E_0}\Delta E = \Gamma_0 + \eta\Delta E \tag{2.67}$$

Substitute equation 2.67 into equation 2.58 and calculate the difference and take the first order Taylor expansion again

$$\delta p = |p_0(E) - p_0(E_0)| = \frac{1}{2} e^{-2\Gamma_0 t} \left| e^{-2\eta \Delta E t} - 1 \right| \approx e^{-2\Gamma_0 t} \eta \Delta E t \tag{2.68}$$

Figure 2.18 qualitatively shows the population difference due to the change $\Delta\Gamma$:

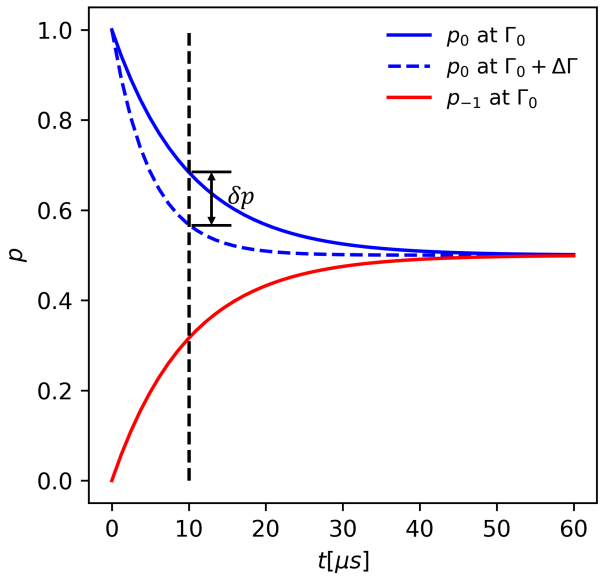

Figure 2.18. Population difference due to $\Delta\Gamma$

Here δp would be our measurement. To evaluate the sensitivity, we need to estimate the error and compare the signal to it, which is the signal-to-noise ratio (SNR).

2.5 Error estimation

The experimental measurement of population p_0 or p_{-1} comes with a non-zero error σ_p. Four sources of the error will be discussed in this section, and we will give an overall estimation of the error afterward.

2.5.1 Quantum projection noise

Quantum projection noise arises from the inherent uncertainty of the quantum sensor. Since the output of the quantum system is probabilistic, we estimate the true probability by the portion of the desired state's occurrence number out of N times of the measurements. For example, the probability of the NV center in $|0\rangle_g$ state is approximated by:

$$p_0 = \frac{N_0}{N} \tag{2.69}$$

where N_0 is the count number of the quantum system (in this work, the state of the effective two level system of the NV center) measured to be in $|0\rangle_g$ state. Such estimation is not accurate until we take infinite times of measurements and the error is given by the variance of the binomial distribution[67] [15]:

$$\sigma^2_{p,quantum} = \frac{1}{N} p(1-p) \tag{2.70}$$

Here we underestimate our accuracy and take the upper bond of the error when $p = 0.5$:

$$\sigma^2_{p,quantum} = \frac{1}{4N} \tag{2.71}$$

2.5.2 Classical readout noise

The readout procedure also introduces noise - the readout results may not be accurately assigned to $|0\rangle_g$ or $|-1\rangle_g$. Depending on the magnitude of the readout error compared to the quantum projection error, we have the single-shot readout noise and averaged readout noise.

When the classical readout noise is relatively small, the histogram of the readout results is broadened but still with two peaks, which is qualitatively shown in Figure 2.19, where x_0 and x_{-1} denote the measurement results corresponding to the quantum state is in $|0\rangle_g$ and $|-1\rangle_g$ while x_T refers to the threshold determining which state a measurement result is to be assigned and is defined as the intersection of the two histogram envelopes. Due

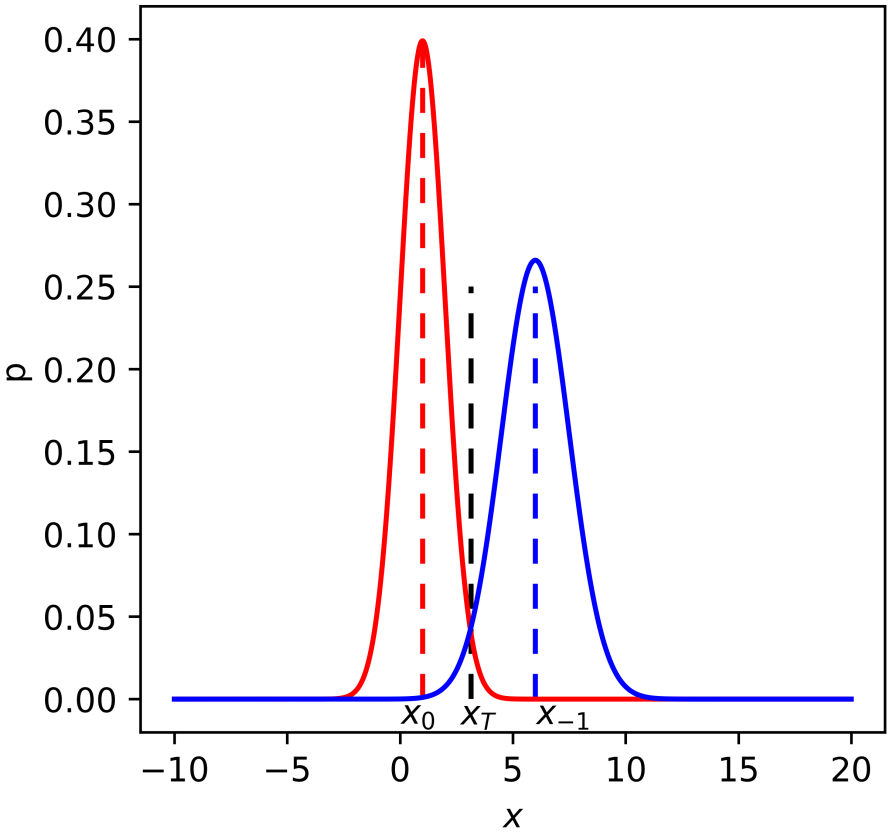

Figure 2.19. Histogram envelope for single-shot readout

to the overlap of the two histograms assumed with Gaussian distribution, there is a finite probability that we assign a result to a wrong state[15]:

$$\kappa_0 \approx \frac{1}{2}\left[1 + erf\left(\frac{|x_0 - x_T|}{\sigma_x}\right)\right] \tag{2.72}$$

where $erf(x)$ is the Gauss error function and κ_0 denotes the ratio of the measurements mistakenly assigned to $|0\rangle_g$ state. Then the error due to wrong assignment[15]:

$$\sigma^2_{p,readout} = \frac{1}{N}[\kappa_0(1-\kappa_0)(1-p_0) + \kappa_{-1}(1-\kappa_{-1})p_0] \tag{2.73}$$

If $\kappa \equiv \kappa_0 \approx \kappa_{-1}$:

$$\sigma^2_{p,readout} \approx \frac{\kappa}{N} \tag{2.74}$$

When the readout noise is large, the histogram shows only one peak so that we cannot assign a measurement to a state. The envelope of the histogram is quanlitatively shown in Figure 2.20. In this case we define the threshold x_T as the average value of all measurements, so the p_0 is evaluated by[15]:

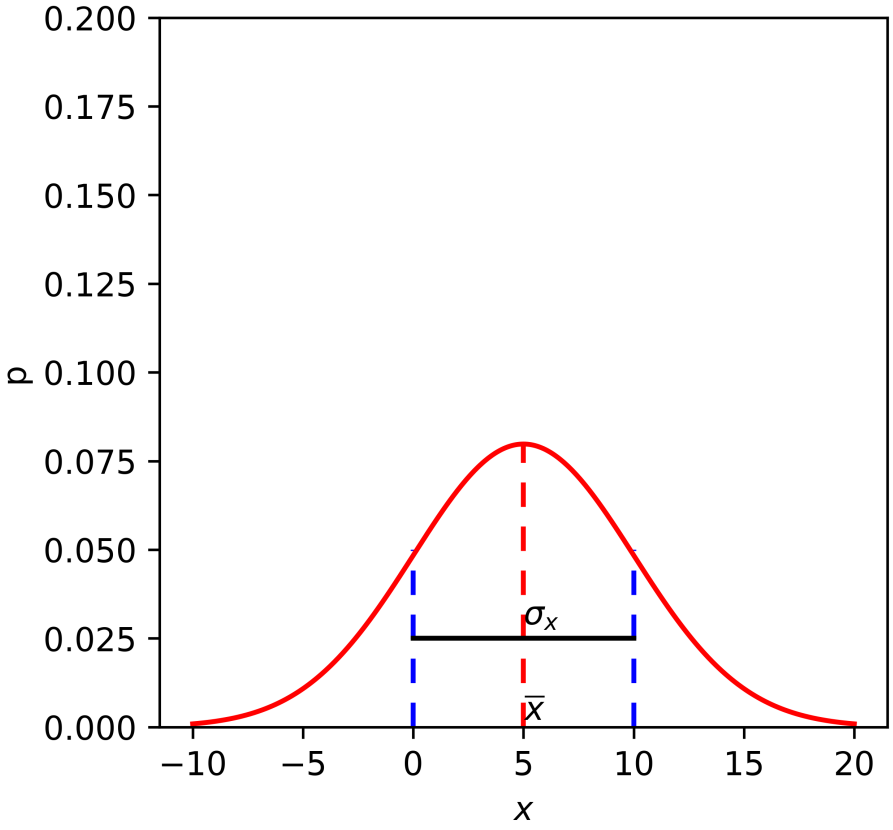

Figure 2.20. Histogram envelope for averaged readout

$$p_0 = \frac{x_{-1} - \bar{x}}{x_{-1} - x_0} \tag{2.75}$$

where $\bar{x}$ is the average value of all measurements. The error of such readout is[15]:

$$\sigma^2_{p,readout} = \frac{\sigma_x^2}{|x_{-1} - x_0|^2} = \frac{R^2}{4N} \tag{2.76}$$

where $|x_{-1} - x_0|$ is the contrast of measurement and R is defined as the ratio between classical readout noise and quantum projection noise:

$$R \equiv \frac{\sigma_{p,readout}}{\sigma_{p,quantum}} = \frac{2\sqrt{N}\sigma_x}{|x_{-1} - x_0|} \tag{2.77}$$

2.5.3 Decoherence

The quantum system suffering from the perturbation in the environment may lose its phase (decoherence) and population (relaxation) information. Typically the signal decays exponentially[15]:

$$\delta p_{obs} = \delta p(t) \mathrm{e}^{-\chi(t)} \tag{2.78}$$

In this work, the population relaxation is exactly utilized for sensing, and we already take this process into account during our derivation of the signal (population difference). So this term will not appear in the overall error estimation.

2.5.4 Error due to initialization and manipulation

The initialization and manipulation of the quantum system may not be perfect and introduce a weakened measurement[15]:

$$\delta p_{obs} = \beta_m \delta p \tag{2.79}$$

where the factor of the signal reduction $\beta_m < 0$ is constant to evolution time t, in this work we will assume $\beta_m = 1$ for simplicity.

2.5.5 Overall error estimation

In this work, we will mainly take the quantum projection noise and classical readout noise into account. For readout noise, we take the worse case - averaged readout for the overall

error estimation. Recall equation 2.77, the quantum projection noise and classical readout noise can be combined as[15]:

$$\sigma_p^2 = \sigma_{p,quantum}^2 + \sigma_{p,readout}^2 \approx (1+R^2)\sigma_{p,quantum}^2 = \frac{\sigma_{p,quantum}^2}{C^2} = \frac{1}{4C^2N} \tag{2.80}$$

where $C = 1/\sqrt{1+R^2}$ is a parameter describing the optical readout efficiency[32]. C is related to the photon collection and detection techniques and can be enhanced to $C \approx 0.3$ in [32] and in this work we will take this value.

Now we have the error and the signal, the whole ingredients for signal-to-noise ratio (SNR), facilitating the sensitivity evaluation.

2.6 SNR and sensitivity

The SNR is defined by the ratio between the signal and the noise:

$$SNR = \frac{\delta p}{\sigma_p} = \mathrm{e}^{-2\Gamma_0 t}\eta\Delta E t 2C\sqrt{N} \tag{2.81}$$

Notice that in this work N is how many cycles of the pulse sequences we undergo. If the total time is T_{tot}, the evolution time is t while the initialization and readout time is t_m, then:

$$N = \frac{T_{tot}}{t+t_m} \tag{2.82}$$

The sensitivity is defined as the minimum signal detectable under a noise ($SNR = 1$) within unit time ($T_{tot} = 1s$):

$$\Delta E_{min} = \frac{\mathrm{e}^{2\Gamma_0 t}\sqrt{t+t_m}}{2C\eta t} \tag{2.83}$$

where $\eta = \frac{d\Gamma}{dE}$. The evaluation of η will be discussed in the methodology and simulation chapter.

Notice that the sensitivity is a function of evolution time and we can optimize it with respect to t by taking the derivative in term of t and extracting the extreme point:

$$t_{min} = \frac{1 - 4\Gamma_0 t_m + \sqrt{1 + 24\Gamma_0 t_m + 16\Gamma_0^2 t_m^2}}{8\Gamma_0} \tag{2.84}$$

By substituting equation 2.84 back to 2.83, we can obtain the sensitivity of the proposed electric field sensor. Since t_{min} is a function of Γ_0, we can further discuss Γ_0 itself in the methodology chapter.

Now we have the full picture of the theory of the sensor and finally derive the expression for the critical figure of merit - sensitivity. The following chapter will discuss the simulation details and exhibit some simulation results.

3. METHODOLOGY

To facilitate the theoretical calculation and numerical simulation in the following chapter, we will discuss the material-related parameters and several details of the calculation and simulation first.

3.1 Material parameters

For the sample using the VCMA effect, we adopt the materials proposed in [59]: The iridium (Ir) doped iron (Fe(001)) is used as the ferromagnet while the MgO(001) layer works as the dielectric material. For magnetoelastic effect, the structure is similar: the amorphous CoFeB film ($H_k = 0$ when there is no strain) is located on the (011) cut PMN-PT substrate[66]. Figure 3.1 shows the dimensions of the system. The NV center is located at $(h_{NV}, L_y/2, L_z/2)$.

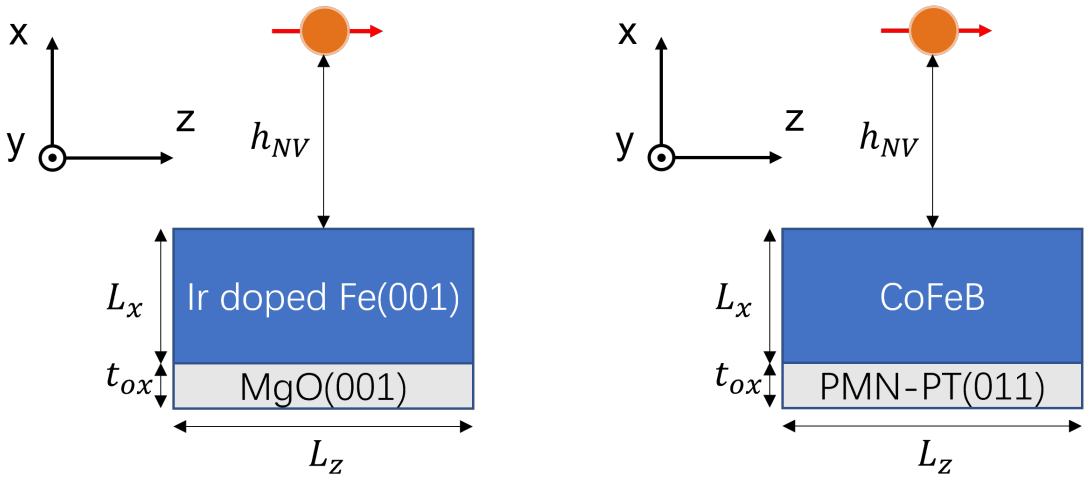

(a) Dimension for VCMA case (b) Dimension for magnetoelastic case

Figure 3.1. Dimension of the sample

The material-related parameters are listed in table 3.1. The thickness for the VCMA effect will be tuned for further investigation of sensitivity - FMR frequency relation, so we will only give the approximate value for L_x and the corresponding conversion coefficient from the electric field to magnetic anisotropy $\xi_{VCMA} = \frac{dH_\perp}{dE}$.

Table 3.1. Material parameters

	VCMA	PMN-PT
$M_s[emu/cc]$	1600	1030
$L_y = L_z[nm]$	400	100
$L_x[nm]$	~ 1	2
α	0.01	0.01
$t_{ox}[nm]$	2	2
$K_V[erg/cc]$	-2×10^7	N.A.
$K_{\mathrm{i}}(0)[erg/cm^2]$	3.7	N.A.
$\beta[erg/(V \cdot cm)]$	320×10^{-10}	N.A.
$\xi_{VCMA} = \frac{dH_\perp}{dE}[Oe/(V/cm)]$	$\sim 4 \times 10^{-4}$	N.A.
$\xi_{PMN-PT} = \frac{dH_k}{dE}[Oe/(V/cm)]$	N.A.	0.027
$H_k[Oe]$	0	0

3.2 Evaluation of η

From the discussion of the propagation of electric field into the change of Γ in section 2.4, we can decompose η by:

$$\frac{d\Gamma}{dE} = \frac{d\Gamma}{d\omega}\frac{d\omega}{dE} \tag{3.1}$$

The former term reflects how much the transition rate is modulated by the shift of FMR frequency, while the latter shows the FMR frequency shifting due to an electric field. Since we already have the expression of ω_{FMR} as a function of E, $\frac{d\omega}{dE}$ can be analytically obtained from equation 2.17. For VCMA (equation 2.63) and PMN-PT (equation 2.65) the forms are different:

$$\begin{aligned}
\frac{d\omega}{dE}_{VCMA} &= \frac{dH_\perp}{dE}\frac{d\omega}{dH_\perp} = \gamma\xi_{VCMA}\frac{H_0 + H_k}{2\sqrt{(H_0 + H_k)(H_0 + H_k + H_\perp)}} \\
\frac{d\omega}{dE}_{PMN-PT} &= \frac{dH_k}{dE}\frac{d\omega}{dH_k} = \gamma\xi_{PMN-PT}\frac{2(H_0 + H_k) + H_\perp}{2\sqrt{(H_0 + H_k)(H_0 + H_k + H_\perp)}}
\end{aligned} \tag{3.2}$$

Then the issue lies in the evaluation of $\frac{d\Gamma}{d\omega}$. Recall Figure 2.17. Assuming that the applied electric field is very small such that the shape of $\tilde{K}(\omega)$ is almost not changed, but the whole

curve is shifted by $\Delta\omega$ (We confirmed the validation of such assumption by Figure 3.2, where we add an extra $10^{-3}H_{\perp} = -0.6Oe$, which is one order higher than the signal-induced anisotropy change), that is, $\tilde{K}'(\omega) = \tilde{K}(\omega+\Delta\omega)$, then the transition rate difference evaluated at $\omega = \epsilon$ is:

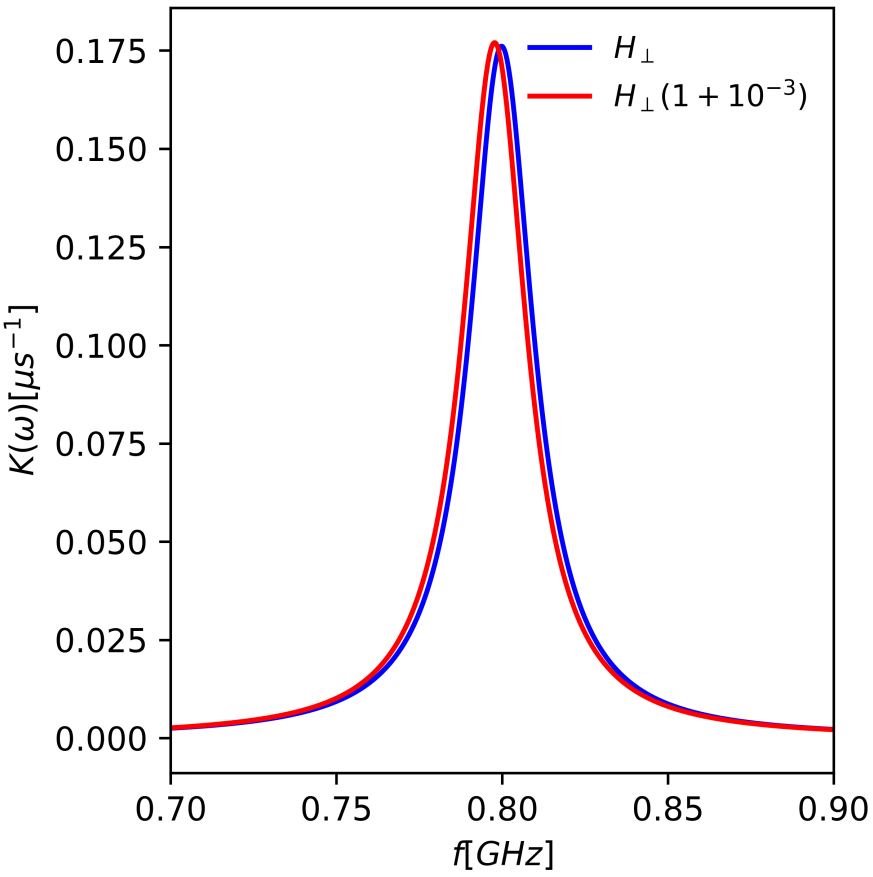

Figure 3.2. Illustration of the validation of the non-reshaped $\tilde{K}(\omega)$

$$\Delta\Gamma = [\tilde{K}(\omega + \Delta\omega) - \tilde{K}(\omega)]|_{\omega=\epsilon} \approx \frac{d\tilde{K}(\omega)}{d\omega}|_{\omega=\epsilon}\Delta\omega \tag{3.3}$$

Hence $\frac{d\Gamma}{d\omega}$ can be evaluated by $\frac{d\tilde{K}(\omega)}{d\omega}|_{\omega=\epsilon}$. For theoretical calculation we can analytically obtain $\frac{d\Gamma}{d\omega}$ while for simulation we need to plot the $\tilde{K}(\omega)$ and evaluate $\frac{d\Gamma}{d\omega}$ by the slope of the curve. Combined with equation 3.2 we can evaluate η and in turn estimate the sensitivity.

3.3 Determine Γ_0

By recalling the expression for the optimum evolution time t_{min} in equation 2.84, we notice that t_{min} is a function of Γ_0. By plotting $t_{min} - \frac{1}{\Gamma_0}$ relation in Figure 3.3 we can check that $t_{min} \approx \frac{1}{4\Gamma_0}$. To determine t_{min}, we can determine the desired Γ_0 by discussing its relation to the initialization and readout time t_m.

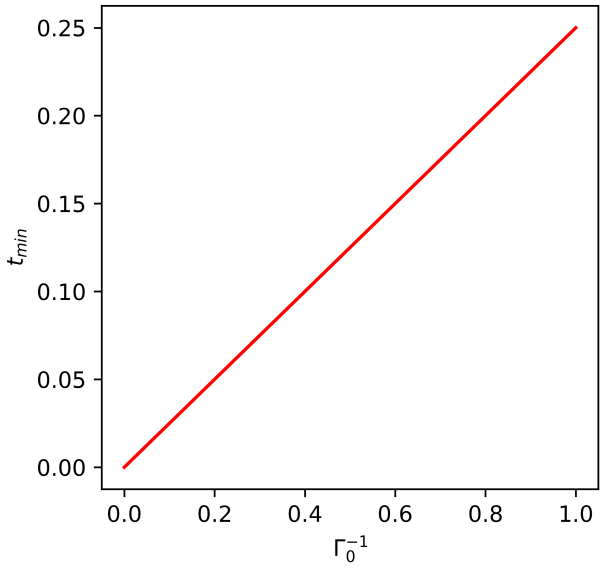

Figure 3.3. t_{min} - $\frac{1}{\Gamma_0}$ relation

Recall the expression of the sensitivity (equation 2.83). Here the slope of the $\tilde{K}(\omega)$ plot, which is a measure of the $\frac{d\Gamma}{d\omega}$, is approximately proportional to $\frac{\Gamma_0}{\alpha\omega}$, where Γ_0 is a measure of the height and $\frac{1}{\alpha\omega}$ is a measure of the width. In this case the sensitivity $\Delta E \sim \sqrt{t + t_m}$. We consider 2 extreme cases:

a. When $\frac{1}{\Gamma_0} \gg t_m$, $t_{min} \gg t_m$, so $\Delta E \sim \sqrt{t} \approx \frac{1}{\sqrt{\Gamma_0}}$, meaning that when Γ_0 is very small, the sensitivity improves with higher transition rate.

b. When $\frac{1}{\Gamma_0} \ll t_m$, $t_{min} \ll t_m$, so $\Delta E \sim \sqrt{t_m}$, which seems to be a constant when Γ_0 is very large. Nevertheless, when taking C into account, too large Γ_0 may introduce significant relaxation before the NV is initialized, rendering a deteriorated C and will still undermine the sensitivity. In this case, the lower transition rate is preferable.

Combining the 2 cases above, we find that a transition rate far from $1/t_m$ is not desired. So in this work, we let $\Gamma_0 = 1/t_m$, where $t_m = 10\mu s$. Practically, we meet such a condition by adjusting the height of NV h_{NV}. We qualitatively illustrate this by Figure 3.4:

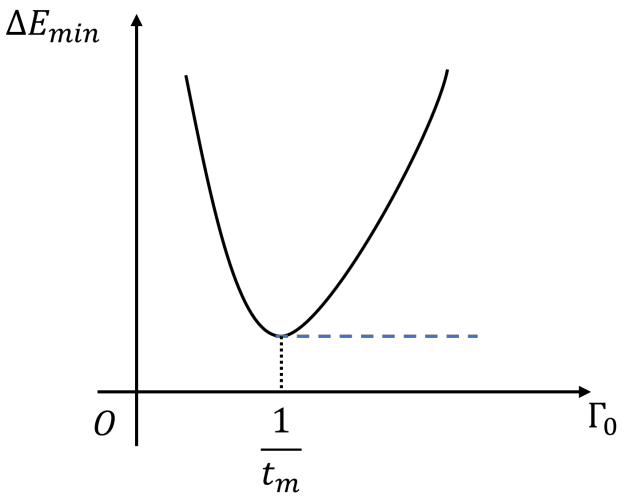

Figure 3.4. The relation between sensitivity and transition rate

3.4 Investigate the sensitivity at different operating frequency

The idea of investigating the relation between ω_{FMR} and the sensitivity arises from $\frac{d\omega}{dE}$. Since we already have ω_{FMR} as a function of E explicitly, we find that with lower ω_{FMR}, $\frac{d\omega}{dE}$ is increasing - this is desirable because it partially enlarges η. But what about the other part $\frac{d\Gamma}{d\omega}$? What is its behavior with lower ω_{FMR}? So we try to let the system work at different ω_{FMR} and see how $\frac{d\Gamma}{d\omega}$ changes accordingly. To vary ω_{FMR} means tuning $H_\perp$ for VCMA case. Considering the thickness-dependent magnetic anisotropy, we can vary the operation frequency by modulating the thickness of the magnet instead of applying a biasing electric field to save energy.

For theoretical calculation in the VCMA case:

1. We first aim at a frequency ω_{FMR} and determine the external field H_0 by the energy splitting of the NV center $\omega_{FMR} = D_{nvg} - \gamma H_0$, which is also the point where we sample the $\tilde{K}(\omega)$ to obtain transition rate Γ.

2. By the expression for the FMR frequency (equation 2.17), solve the $H_\perp$.

3. Then obtain the thickness of the ferromagnet L_x by the expression for VCMA-modulated $H_\perp$ (equation 2.62).

4. Evaluate the sensitivity by analytically figuring out $\frac{d\Gamma}{d\omega}$ and $\frac{d\omega}{dE}$ at such operation frequency.

For numerical simulation of the VCMA case, the first three steps are the same. For the fourth step, the evaluation of $\frac{d\Gamma}{d\omega}$ is different:

1. A Runge-Kutta LLG solver is used to obtain magnetization dynamics $\delta m'_{\mathrm{i}}$ under the thermal noise.

2. The power spectrum of the magnetization C_{ij} is obtained by first calculating the correlation functions in time domain $\langle \delta m'_{\mathrm{i}} \delta m'_{\mathrm{j}} \rangle$ and doing fast Fourier transform.

3. Using the rotated version $\bar{B}$ matrix elements we construct $\tilde{K}(\omega)$ by linear combinations of C_{ij}.

4. A smoothing procedure is conducted by firstly down-sampling using a Fourier method (scipy.signal.resample in python) and then interpolating with a polynomial (scipy.interpolate.UnivariateSpli in python) with smoothing factor $s = 10^8$.

The simulation related parameters are: $T = 300K$, simulation time $T_{sim} = 5\mu s$, time step $dT = 10ps$. The simulation is repeated for 100 times and we take the average.

Now we have been through all the theoretical basis and details of the simulation. Next chapter, we will demonstrate some simulation results and compare them with the theoretical calculation.

4. SIMULATION RESULTS

In this chapter, we will exhibit the figures of $\tilde{K}(\omega)$ for both theoretical calculation and simulation results. The estimated sensitivity will be given accordingly. We will focus on the VCMA results and compare the sensitivity ΔE_{min} to the magnetoelastic effect case later.

The simulation results (solid cyan line), sampled data from simulation results (red dot), polynomial fitting curves (dot-dash black line), and theoretical results (solid blue line) at operation frequencies from $1.8GHz$ to $0.6GHz$ for VCMA effect case are shown in Figure 4.1:

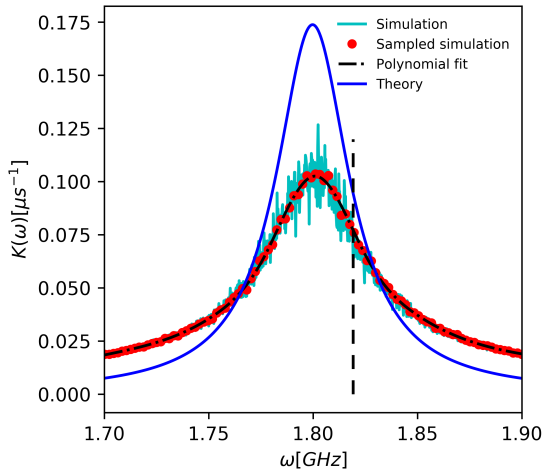

(a) $\tilde{K}(\omega)$ at $\omega_{FMR} = 1.8GHz$ for VCMA

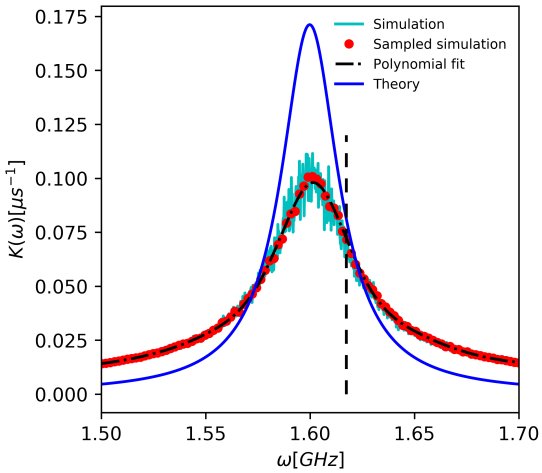

(b) $\tilde{K}(\omega)$ at $\omega_{FMR} = 1.6GHz$ for VCMA

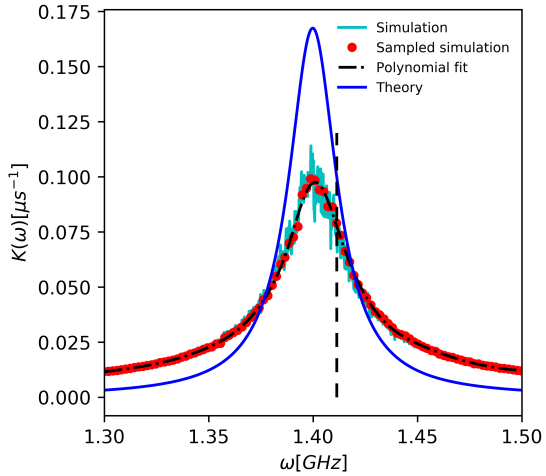

(c) $\tilde{K}(\omega)$ at $\omega_{FMR} = 1.4GHz$ for VCMA

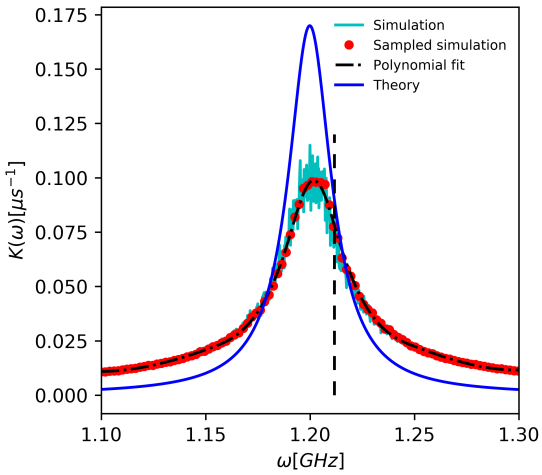

(d) $\tilde{K}(\omega)$ at $\omega_{FMR} = 1.2GHz$ for VCMA

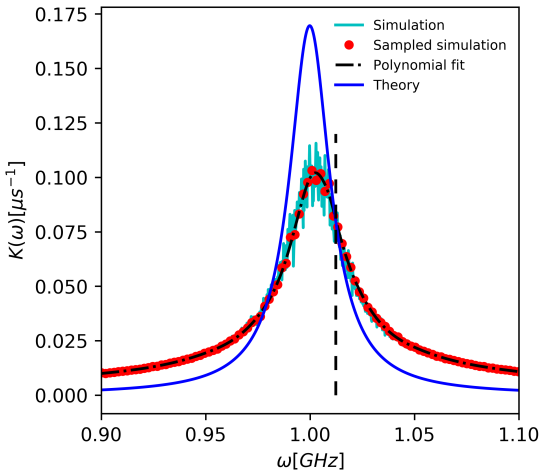

(e) $\tilde{K}(\omega)$ at $\omega_{FMR} = 1.0GHz$ for VCMA

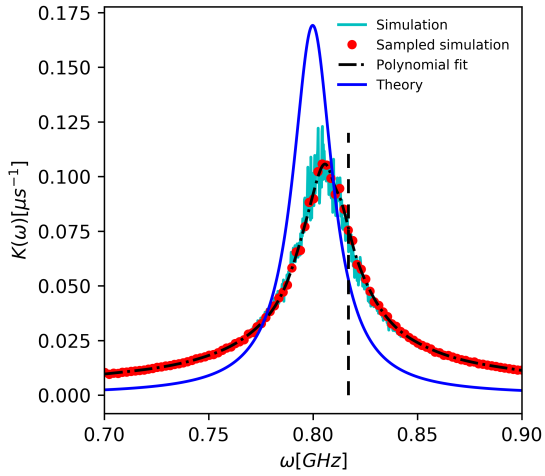

(f) $\tilde{K}(\omega)$ at $\omega_{FMR} = 0.8GHz$ for VCMA

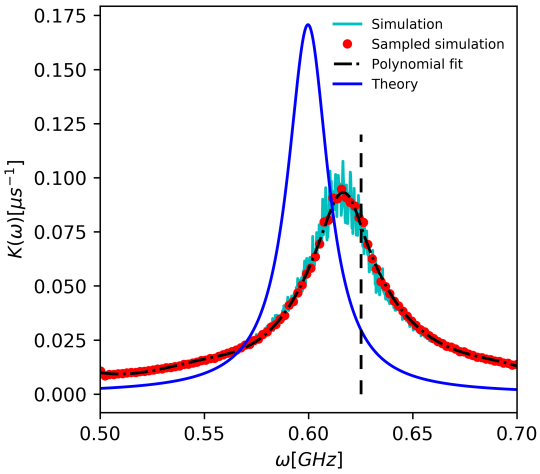

(g) $\tilde{K}(\omega)$ at $\omega_{FMR} = 0.6GHz$ for VCMA

Figure 4.1. VCMA simulation results at differint FMR frequency

By looking at the theoretical results, the heights of the peaks almost remain the same. This arises from the adjustment of NV height to make sure $\Gamma_0 \sim 1/t_m$ (recall section 3.3). However, the shapes become narrower with lower frequency - intuitively, we can say that the slopes $\frac{d\tilde{K}(\omega)}{d\omega}$, an approximation of $\frac{d\Gamma}{d\omega}$, increases with lower ω_{FMR}. Such a trend exists in the simulation results, too. This means that reducing ω_{FMR} can improve both $\frac{d\Gamma}{d\omega}$ and $\frac{d\omega}{dE}$. As a result, we expect the sensitivity to be enhanced with lower FMR frequency. Comparing simulation and theoretical results, we find that the peaks of the simulation results are lower than the theoretical ones, and the peak frequencies of theoretical and simulation results match

well at first but gradually deviate from each other with lower frequencies. We summarize some observations of the trends in Table 4.1 and will plot some interesting parameters later.

Table 4.1. Summary results for VCMA

$\omega_{FMR}[GHz]$	0.6	0.8	1.0	1.2	1.4	1.6	1.8
$\frac{d\Gamma}{d\omega}_{theory}[\times 10^{-3}]$	8.487	8.561	8.442	7.952	6.981	5.955	4.690
$\frac{d\Gamma}{d\omega}_{simulation}[\times 10^{-3}]$	2.633	3.972	3.667	3.316	2.964	2.330	2.059
$\frac{d\omega}{dE}[Hz/(V/cm)]$	2034.841	1383.539	992.758	732.237	546.151	406.586	298.036
$s_{theory}[V/(cm\cdot\sqrt{Hz})]$	202.240	293.809	416.811	600.844	905.704	1443.877	2505.781
$s_{simulation}[V/(cm\cdot\sqrt{Hz})]$	646.572	630.178	951.613	1426.300	2139.124	3654.944	5642.781
$d_F[nm]$	1.009088	1.011898	1.015354	1.019706	1.025358	1.032991	1.043872
$h_{NV}[nm]$	263	223	190	160	131	95	45

Table 4.1 assembles some results from the figures above. We find that with the reduction of the operation frequency, whether for theory or simulation results, both the $\frac{d\Gamma}{d\omega}$ and $\frac{d\omega}{dE}$ increase and cause enhanced sensitivity. To visualize such trends, we first try to plot the relation between $\frac{d\omega}{dE}$ and ω_{FMR} in Figure 4.2(a). Figure 4.2(a) shows that $\frac{d\omega}{dE}$ may have an

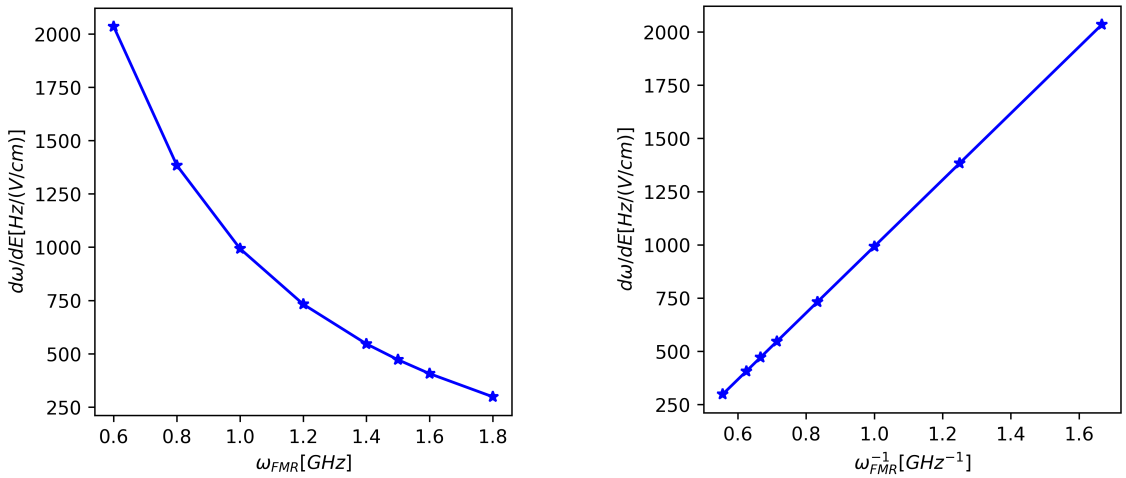

(a) $\frac{d\omega}{dE} - \omega_{FMR}$ relation

(b) $\frac{d\omega}{dE} - \omega_{FMR}^{-1}$ relation

Figure 4.2. Exploring the relation between $\frac{d\omega}{dE}$ and ω_{FMR}

inverse-like relation to ω_{FMR}, that is, $\frac{d\omega}{dE} \sim \omega_{FMR}^{-n}$. By trying $n = 1$ we plot the $\frac{d\omega}{dE}$ against ω_{FMR}^{-1} in Figure 4.2(b) and it has very good linearity. So we can say $\frac{d\omega}{dE} \sim \omega_{FMR}^{-1}$.

However, the relation between $\frac{d\Gamma}{d\omega}$ and ω_{FMR} is relatively complicated and is plotted in Figure 4.3. Whether for theoretical and simulation results, $\frac{d\Gamma}{d\omega}$ increases with a lower frequency and almost saturates at low frequencies (except for $\omega_{FMR} = 0.6$GHz), which coincides with our previous observation.

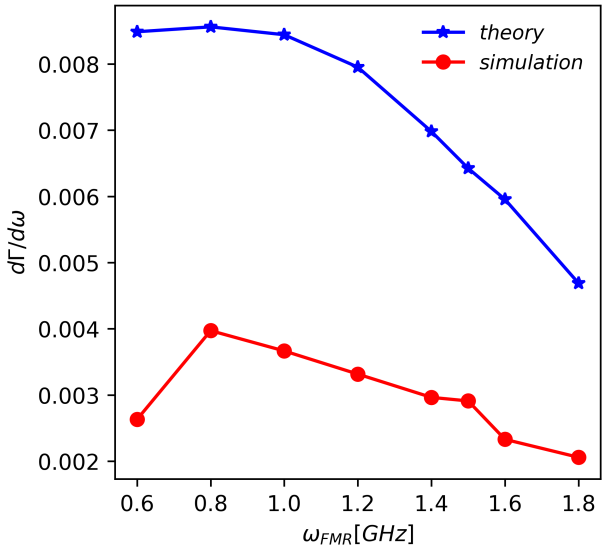

Figure 4.3. $\frac{d\Gamma}{d\omega} - \omega_{FMR}$ relation

Based on the trends we show in Figure 4.2 and 4.3, lowering ω_{FMR} contributes to not only higher $\frac{d\omega}{dE}$ but also better $\frac{d\Gamma}{d\omega}$. As the product of these two parameters, $\frac{d\Gamma}{dE}$ increases with lower FMR frequency and results in better sensitivity. The sensitivity - ω_{FMR} relation is illustrated in Figure 4.4(a) for VCMA case:

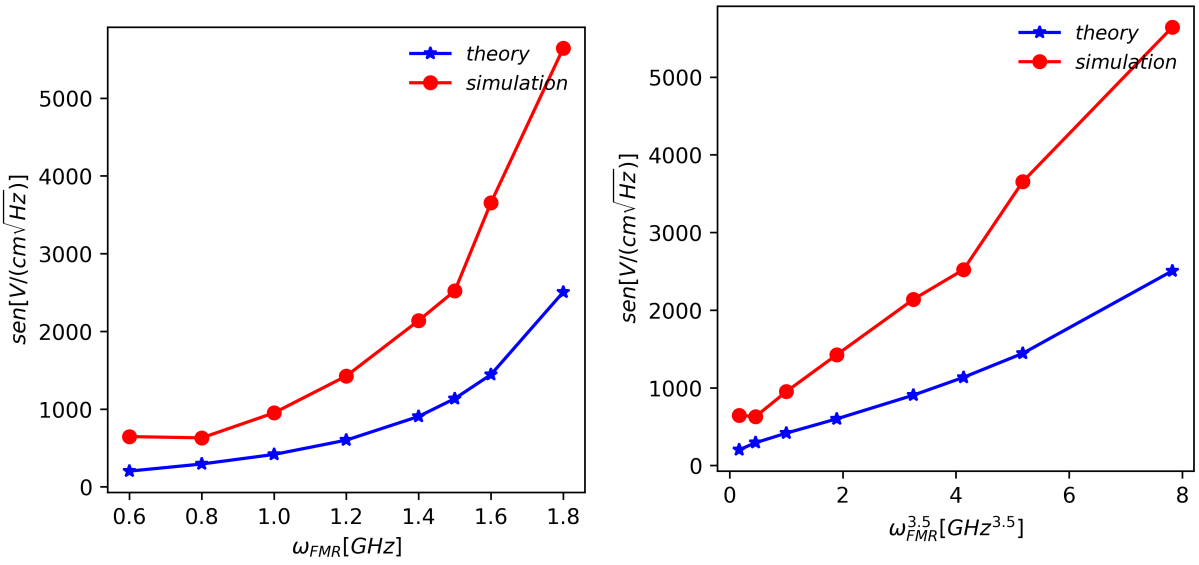

(a) sensitivity - ω_{FMR} relation for VCMA, sensitivity is improving with lower frequency

(b) sensitivity - $\omega_{FMR}^{3.5}$ relation for VCMA, the sensitivity is approximately proportional to $\omega_{FMR}^{3.5}$

Figure 4.4. Exploring the relation between sensitivity and ω_{FMR}

Such relation is like $\Delta E \sim \omega_{FMR}^{n}$, by several trying we find that when $n = 3.5$, the consequent curve shows good linearity. Given Figure 4.4(b), we can say the sensitivity can be enhanced by tuning the operation frequency, and such adjustment can be made by using ferromagnet with different thicknesses. Meanwhile, from Table 4.1, we can find that even if the ω_{FMR} changes by over $1GHz$, the corresponding thickness only varies about $0.03nm$. Such a phenomenon indicates that the magnet material may be susceptible to its shape, which is utilized by the electric-field-induced magnetoelastic effect using PMN-PT.

The calculation and simulation for PMN-PT have been done in [66]. With the sensitivity $\Delta E \approx 5.3V/(cm \cdot \sqrt{Hz})$, it outperforms the VCMA case in this work ($\Delta E \approx 200V/(cm \cdot \sqrt{Hz})$) for two orders of magnitude. Following, we would like to compare some parameters between VCMA and PMN-PT to figure out the reason.

Recall the evaluation of η:

$$\frac{d\Gamma}{dE} = \frac{d\Gamma}{d\omega}\frac{d\omega}{dE} \tag{4.1}$$

In this expression, we decompose the coupling of transition rate to electric field into two parts. The first term describes how the quantum system (in our case, the NV center) will

respond to the noisy magnetic field, corresponding to the NV part. For both schemes using the NV center, such NV-dependent $\frac{d\Gamma}{d\omega}$ should not make a significant difference. However, for the magnet part, $\frac{d\omega}{dE}$ shows different behaviors. By equation 3.2, the parameter ξ_{VCMA} and ξ_{PMN-PT} play an important role. Table 3.1 includes these two parameters, and ξ_{PMN-PT} is about two orders higher than ξ_{VCMA}, which partially accounts for the two orders of better performance. Besides, since in PMN-PT case, the modulated H_k enters both of the frequency components ω_H and $\omega_\perp$, it has greater $\frac{d\omega}{dH_k}$ than $\frac{d\omega}{dH_\perp}$ for VCMA, which is shown in equation 3.2.

We put the dc electric field sensitivity obtained by Stark effect using single NV center, VCMA effect, and magnetoelastic effect together for comparison:

Table 4.2. Comparison among the sensitivity using Stark, VCMA, and Magnetoelastic effects

	Stark(single NV)	VCMA	Magnetoelastic
$\Delta E_{min}[V/(cm \cdot \sqrt{Hz})]$	891	~ 200	~ 1

Here we must have two questions:

1. Why are the peak frequencies of theoretical calculation and simulation not matched?
2. Why do the simulation results show much lower peak height?

For these two questions, one possible reason lies in the total simulation time. In Figure 4.5, we demonstrate the results for $\omega_{FMR} = 0.8GHz$, by keeping all the parameters the same while only varying total simulation time from $1\mu s$ to $5\mu s$. We can see that for most of the cases except for $3\mu s$, the magnitude of $\tilde{K}(\omega)$ increases with longer total simulation time. Meanwhile, the frequency mismatch between theoretical and simulation results declines when the simulation time increases. From this trend, we can expect that the simulation time will approach the theoretical result when the simulation time is long enough. Here we give the simulation result up to $5\mu s$ because longer simulation time becomes infeasible.

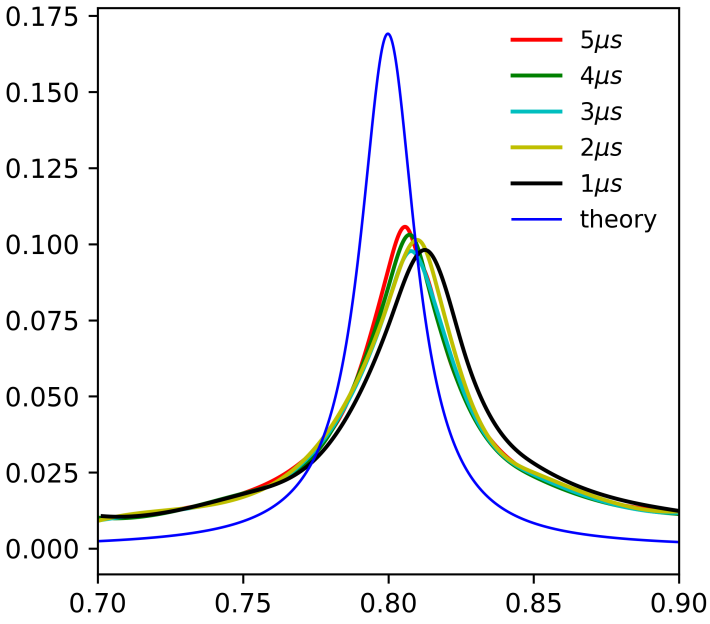

Figure 4.5. $\tilde{K}(\omega)$ for simulation time $1\mu s \sim 5\mu s$: with longer simulation time, the peaks of $\tilde{K}(\omega)$ (except for $3\mu s$) increase and the frequencies also approach the theory curve

Another explanation is the validation of the linearized LLG equation. For theoretical derivation, we assumed that the thermal field is tiny such that we can omit the higher-order terms in the original LLG equation. Recall the correlator of the thermal field $D_{th} = \frac{\alpha k_B T}{M_s V}$, where V is the volume of the magnet. At room temperature, if the given material has a tiny volume, chances are that the thermal noise may be large enough so that the higher-order terms take effect and introduce frequency shift. When temperature and material are fixed, a larger volume is expected to mitigate such effect but at the expense of spatial resolution. To check whether linearized LLG equation is still valid we plot the magnetization dynamics in time domain for operation frequency $\omega_{FMR} = 1.8GHz$ and $\omega_{FMR} = 0.8GHz$ in Figure 4.6. The largest fluctuation magnitude for $\omega_{FMR} = 0.8GHz$ is 0.1 while for $\omega_{FMR} = 1.8GHz$ it is 0.025. In this case, the linearized LLG equation still applies.

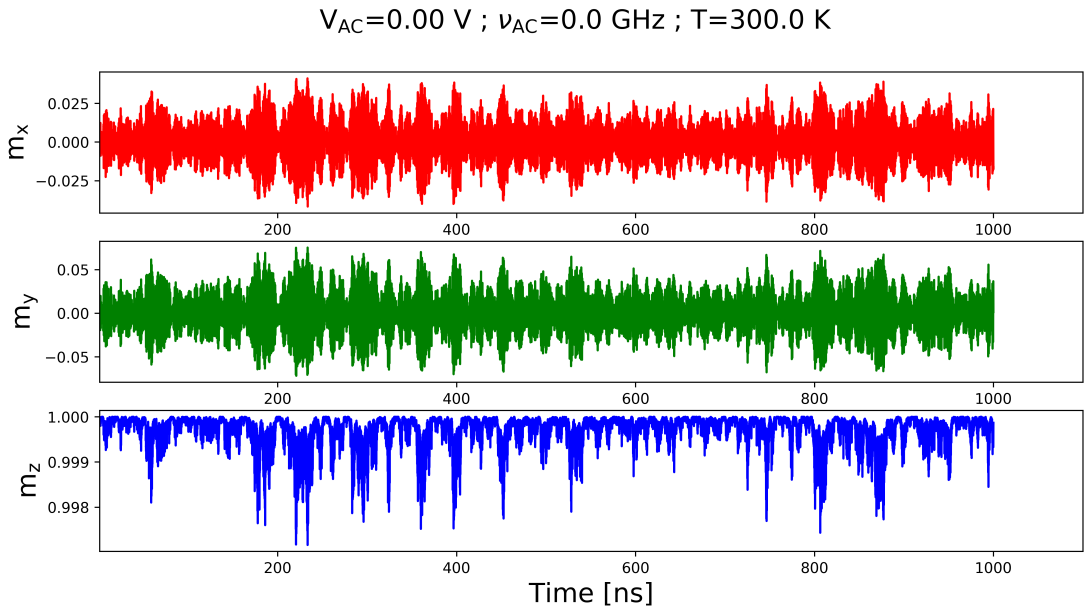

(a) Magnetization dynamics at $\omega_{FMR} = 1.8GHz$ for VCMA, the largest deviation for m_x is about 0.025

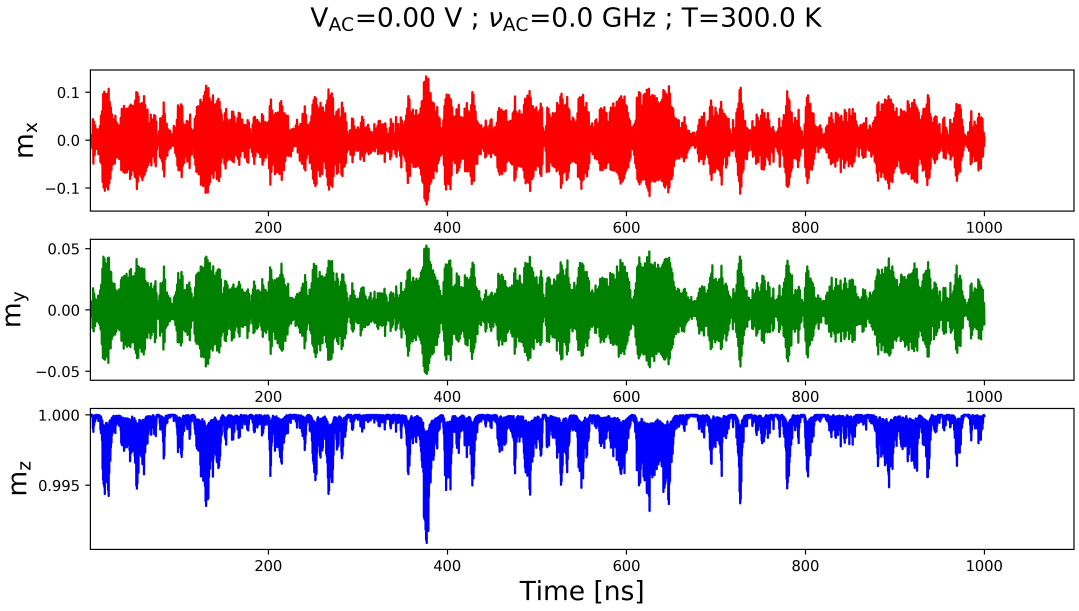

(b) Magnetization dynamics at $\omega_{FMR} = 0.8GHz$ for VCMA, the largest deviation for m_x is about 0.1

Figure 4.6. Magnetization dynamics for $\omega_{FMR} = 1.8GHz$ and $\omega_{FMR} = 0.8GHz$

Now we have gone over the main body of this work (theory, methodology, and results). We will conclude and give some outlook in the following chapter.

5. CONCLUSION

In this thesis, we propose an electric field sensor using the population relaxation of an NV center. To overcome the NV center's inherent weak coupling to the electric field, we try to convert the electric field into the magnetic property modulation of a ferromagnet. Consequently, the shifted power spectrum of the magnetic noise at the NV center renders a different transition rate, facilitating the population difference measurement. Compared to other sensing protocols, the pulse sequence of the relaxometry is very simple, and the absence of a microwave leads to less power consumption. The room-temperature operation and easy external magnetic field source (a permanent magnet) contribute to the simple lab configuration. Since the magnetic noise arises from finite temperature, such a scheme can also work as a temperature sensor.

The proposed sensor allows us to improve the sensitivity by trying different compositions of materials with higher conversion coefficients from electric fields to magnetic properties. In this work, the PMN-PT case combines the piezoelectric and magnetoelastic effect, showing much superior electric-field modulation of magnetic anisotropy. This work also investigates the sensitivities at different FMR frequencies and reveals that working at a lower FMR frequency is preferable for better sensitivity. Compared to the early electric field sensing work using single NV center[34], our sensor exhibits improved sensitivity, but still far from two recent works [35] [36]. All these three sensors take advantage of direct coupling to the electric field (Stark effect), but later two employ NV ensembles and achieve the sensitivity improvement by order of $\sim 10^3$ or more. Considering the single NV we are using, NV ensembles are expected to enhance our performance. Overall, there remains a lot to do in quantum sensing to explore its potential for more fundamental insight into the quantum world and versatile applications in our lives.

REFERENCES

[1] W. S. Boyle and G. E. Smith, "Charge coupled semiconductor devices," *The Bell System Technical Journal*, vol. 49, no. 4, pp. 587–593, 1970. DOI: 10.1002/j.1538-7305.1970.tb01790.x.

[2] R. Widlar, "An exact expression for the thermal variation of the emitter base voltage of bi-polar transistors," *Proceedings of the IEEE*, vol. 55, no. 1, pp. 96–97, 1967. DOI: 10.1109/PROC.1967.5396.

[3] K. M. Tyner, R. Kopelman, and M. A. Philbert, ""nanosized voltmeter" enables cellular-wide electric field mapping," *Biophysical Journal*, vol. 93, no. 4, pp. 1163–1174, 2007, ISSN: 0006-3495. DOI: https://doi.org/10.1529/biophysj.106.092452. [Online]. Available: https://www.sciencedirect.com/science/article/pii/S0006349507713747.

[4] E. National Academies of Sciences and Medicine, *Quantum Computing: Progress and Prospects*, E. Grumbling and M. Horowitz, Eds. Washington, DC: The National Academies Press, 2019, ISBN: 978-0-309-47969-1. DOI: 10.17226/25196. [Online]. Available: https://www.nap.edu/catalog/25196/quantum-computing-progress-and-prospects.

[5] A. Jarmola, V. M. Acosta, K. Jensen, S. Chemerisov, and D. Budker, "Temperature- and magnetic-field-dependent longitudinal spin relaxation in nitrogen-vacancy ensembles in diamond," *Phys. Rev. Lett.*, vol. 108, p. 197 601, 19 May 2012. DOI: 10.1103/PhysRevLett.108.197601. [Online]. Available: https://link.aps.org/doi/10.1103/PhysRevLett.108.197601.

[6] E. Bauch, S. Singh, J. Lee, *et al.*, "Decoherence of ensembles of nitrogen-vacancy centers in diamond," *Phys. Rev. B*, vol. 102, p. 134 210, 13 Oct. 2020. DOI: 10.1103/PhysRevB.102.134210. [Online]. Available: https://link.aps.org/doi/10.1103/PhysRevB.102.134210.

[7] I. Kominis, T. Kornack, J. Allred, and M. V. Romalis, "A subfemtotesla multichannel atomic magnetometer," *Nature*, vol. 422, no. 6932, pp. 596–599, 2003.

[8] M. Balabas, T. Karaulanov, M. Ledbetter, and D. Budker, "Polarized alkali-metal vapor with minute-long transverse spin-relaxation time," *Physical review letters*, vol. 105, no. 7, p. 070 801, 2010.

[9] H. Dang, A. C. Maloof, and M. V. Romalis, "Ultrahigh sensitivity magnetic field and magnetization measurements with an atomic magnetometer," *Applied Physics Letters*, vol. 97, no. 15, p. 151 110, 2010.

[10] D. Budker and M. Romalis, "Optical magnetometry," *Nature physics*, vol. 3, no. 4, pp. 227–234, 2007.

[11] V. Shah, S. Knappe, P. D. Schwindt, and J. Kitching, "Subpicotesla atomic magnetometry with a microfabricated vapour cell," *Nature Photonics*, vol. 1, no. 11, pp. 649–652, 2007.

[12] R. Maiwald, D. Leibfried, J. Britton, J. C. Bergquist, G. Leuchs, and D. J. Wineland, "Stylus ion trap for enhanced access and sensing," *Nature Physics*, vol. 5, no. 8, pp. 551–554, 2009.

[13] M. J. Biercuk, H. Uys, J. W. Britton, A. P. VanDevender, and J. J. Bollinger, "Ultrasensitive detection of force and displacement using trapped ions," *Nature nanotechnology*, vol. 5, no. 9, pp. 646–650, 2010.

[14] I. Baumgart, J.-M. Cai, A. Retzker, M. B. Plenio, and C. Wunderlich, "Ultrasensitive magnetometer using a single atom," *Physical review letters*, vol. 116, no. 24, p. 240 801, 2016.

[15] C. L. Degen, F. Reinhard, and P. Cappellaro, "Quantum sensing," *Reviews of modern physics*, vol. 89, no. 3, p. 035 002, 2017.

[16] M. Brownnutt, M. Kumph, P. Rabl, and R. Blatt, "Ion-trap measurements of electric-field noise near surfaces," *Reviews of modern Physics*, vol. 87, no. 4, p. 1419, 2015.

[17] M. Simmonds, W. Fertig, and R. Giffard, "Performance of a resonant input squid amplifier system," *IEEE Transactions on Magnetics*, vol. 15, no. 1, pp. 478–481, 1979. DOI: 10.1109/TMAG.1979.1060155.

[18] A. Kraft, C. Rupprecht, and Y.-C. Yam, *Superconducting quantum interference device (squid)*, 2017.

[19] D. Vasyukov, Y. Anahory, L. Embon, *et al.*, "A scanning superconducting quantum interference device with single electron spin sensitivity," *Nature nanotechnology*, vol. 8, no. 9, pp. 639–644, 2013.

[20] F. Casola, T. van der Sar, and A. Yacoby, "Probing condensed matter physics with magnetometry based on nitrogen-vacancy centres in diamond," *Nature Reviews Materials*, vol. 3, no. 1, pp. 1–13, 2018.

[21] R. Amsüss, C. Koller, T. Nöbauer, *et al.*, "Cavity qed with magnetically coupled collective spin states," *Physical review letters*, vol. 107, no. 6, p. 060 502, 2011.

[22] M. Pelliccione, A. Jenkins, P. Ovartchaiyapong, *et al.*, "Scanned probe imaging of nanoscale magnetism at cryogenic temperatures with a single-spin quantum sensor," *Nature nanotechnology*, vol. 11, no. 8, pp. 700–705, 2016.

[23] D. Toyli, D. Christle, A. Alkauskas, B. Buckley, C. Van de Walle, and D. Awschalom, "Measurement and control of single nitrogen-vacancy center spins above 600 k," *Physical Review X*, vol. 2, no. 3, p. 031 001, 2012.

[24] R. Schirhagl, K. Chang, M. Loretz, and C. L. Degen, "Nitrogen-vacancy centers in diamond: Nanoscale sensors for physics and biology," *Annual review of physical chemistry*, vol. 65, pp. 83–105, 2014.

[25] J. Tisler, G. Balasubramanian, B. Naydenov, *et al.*, "Fluorescence and spin properties of defects in single digit nanodiamonds," *ACS nano*, vol. 3, no. 7, pp. 1959–1965, 2009.

[26] A. S. Barnard, "Diamond standard in diagnostics: Nanodiamond biolabels make their mark," *Analyst*, vol. 134, no. 9, pp. 1751–1764, 2009.

[27] A. Gruber, A. Dräbenstedt, C. Tietz, L. Fleury, J. Wrachtrup, and C. Von Borczyskowski, "Scanning confocal optical microscopy and magnetic resonance on single defect centers," *Science*, vol. 276, no. 5321, pp. 2012–2014, 1997.

[28] C. Kurtsiefer, S. Mayer, P. Zarda, and H. Weinfurter, "Stable solid-state source of single photons," *Physical review letters*, vol. 85, no. 2, p. 290, 2000.

[29] T. Wolf, P. Neumann, K. Nakamura, *et al.*, "Subpicotesla diamond magnetometry," *Physical Review X*, vol. 5, no. 4, p. 041 001, 2015.

[30] J. R. Maze, P. L. Stanwix, J. S. Hodges, *et al.*, "Nanoscale magnetic sensing with an individual electronic spin in diamond," *Nature*, vol. 455, no. 7213, pp. 644–647, 2008.

[31] M. S. Grinolds, S. Hong, P. Maletinsky, *et al.*, "Nanoscale magnetic imaging of a single electron spin under ambient conditions," *Nature Physics*, vol. 9, no. 4, pp. 215–219, 2013.

[32] J. Taylor, P. Cappellaro, L. Childress, *et al.*, "High-sensitivity diamond magnetometer with nanoscale resolution," *Nature Physics*, vol. 4, no. 10, pp. 810–816, 2008.

[33] E. Van Oort and M. Glasbeek, "Electric-field-induced modulation of spin echoes of nv centers in diamond," *Chemical Physics Letters*, vol. 168, no. 6, pp. 529–532, 1990.

[34] F. Dolde, H. Fedder, M. W. Doherty, *et al.*, "Electric-field sensing using single diamond spins," *Nature Physics*, vol. 7, no. 6, pp. 459–463, 2011.

[35] E. H. Chen, H. A. Clevenson, K. A. Johnson, *et al.*, "High-sensitivity spin-based electrometry with an ensemble of nitrogen-vacancy centers in diamond," *Physical Review A*, vol. 95, no. 5, p. 053 417, 2017.

[36] M. Block, B. Kobrin, A. Jarmola, *et al.*, "Optically enhanced electric field sensing using nitrogen-vacancy ensembles," *Physical Review Applied*, vol. 16, no. 2, p. 024 024, 2021.

[37] J. Michl, J. Steiner, A. Denisenko, *et al.*, "Robust and accurate electric field sensing with solid state spin ensembles," *Nano letters*, vol. 19, no. 8, pp. 4904–4910, 2019.

[38] R. Li, F. Kong, P. Zhao, *et al.*, "Nanoscale electrometry based on a magnetic-field-resistant spin sensor," *Physical Review Letters*, vol. 124, no. 24, p. 247 701, 2020.

[39] C. Kittel, "On the theory of ferromagnetic resonance absorption," *Physical review*, vol. 73, no. 2, p. 155, 1948.

[40] D. D. Stancil and A. Prabhakar, *Spin waves*. Springer, 2009, vol. 5.

[41] W. F. Brown, "Thermal fluctuations of a single-domain particle," *Phys. Rev.*, vol. 130, pp. 1677–1686, 5 Jun. 1963. DOI: 10.1103/PhysRev.130.1677. [Online]. Available: https://link.aps.org/doi/10.1103/PhysRev.130.1677.

[42] R. Kubo and N. Hashitsume, "Brownian Motion of Spins," *Progress of Theoretical Physics Supplement*, vol. 46, pp. 210–220, Jun. 1970, ISSN: 0375-9687. DOI: 10.1143/PTPS.46.210. [Online]. Available: https://doi.org/10.1143/PTPS.46.210.

[43] A. Rustagi, I. Bertelli, T. van der Sar, and P. Upadhyaya, "Sensing chiral magnetic noise via quantum impurity relaxometry," *Phys. Rev. B*, vol. 102, p. 220 403, 22 Dec. 2020. DOI: 10.1103/PhysRevB.102.220403.

[44] R. Engel-Herbert and T. Hesjedal, "Calculation of the magnetic stray field of a uniaxial magnetic domain," *Journal of Applied Physics*, vol. 97, no. 7, p. 074 504, 2005.

[45] J. Norpoth, S. Dreyer, and C. Jooss, "Straightforward field calculations for uniaxial hardmagnetic prisms: Stray field distributions and dipolar coupling in regular arrays," *Journal of Physics D: Applied Physics*, vol. 41, no. 2, p. 025 001, 2007.

[46] L. Trifunovic, F. L. Pedrocchi, S. Hoffman, P. Maletinsky, A. Yacoby, and D. Loss, "High-efficiency resonant amplification of weak magnetic fields for single spin magnetometry at room temperature," *Nature nanotechnology*, vol. 10, no. 6, pp. 541–546, 2015.

[47] M. W. Doherty, N. B. Manson, P. Delaney, F. Jelezko, J. Wrachtrup, and L. C. Hollenberg, "The nitrogen-vacancy colour centre in diamond," *Physics Reports*, vol. 528, no. 1, pp. 1–45, 2013.

[48] Y. Chu and M. D. Lukin, "Quantum optics with nitrogen-vacancy centres in diamond," in ser. Quantum Optics and Nanophotonics. Oxford: Oxford University Press, 2017, ISBN: 9780198768609. DOI: 10.1093/oso/9780198768609.003.0005.

[49] T. Engel and P. Reid, *Physical Chemistry*. Pearson Benjamin Cummings, 2006, ISBN: 9780805338423. [Online]. Available: https://books.google.com/books?id=GmUvAQAAIAAJ.

[50] D. A. Hopper, H. J. Shulevitz, and L. C. Bassett, "Spin readout techniques of the nitrogen-vacancy center in diamond," *Micromachines*, vol. 9, no. 9, 2018, ISSN: 2072-666X. DOI: 10.3390/mi9090437. [Online]. Available: https://www.mdpi.com/2072-666X/9/9/437.

[51] M. L. Goldman, M. W. Doherty, A. Sipahigil, *et al.*, "State-selective intersystem crossing in nitrogen-vacancy centers," *Phys. Rev. B*, vol. 91, p. 165 201, 16 Apr. 2015. DOI: 10.1103/PhysRevB.91.165201. [Online]. Available: https://link.aps.org/doi/10.1103/PhysRevB.91.165201.

[52] A. Gupta, L. Hacquebard, and L. Childress, "Efficient signal processing for time-resolved fluorescence detection of nitrogen-vacancy spins in diamond," *J. Opt. Soc. Am. B*, vol. 33, no. 3, B28–B34, Mar. 2016. DOI: 10.1364/JOSAB.33.000B28. [Online]. Available: http://www.osapublishing.org/josab/abstract.cfm?URI=josab-33-3-B28.

[53] D. A. Hopper, R. R. Grote, A. L. Exarhos, and L. C. Bassett, "Near-infrared-assisted charge control and spin readout of the nitrogen-vacancy center in diamond," *Phys. Rev. B*, vol. 94, p. 241 201, 24 Dec. 2016. DOI: 10.1103/PhysRevB.94.241201. [Online]. Available: https://link.aps.org/doi/10.1103/PhysRevB.94.241201.

[54] A. Gupta, L. Hacquebard, and L. Childress, "Efficient signal processing for time-resolved fluorescence detection of nitrogen-vacancy spins in diamond," *JOSA B*, vol. 33, no. 3, B28–B34, 2016.

[55] F. Jelezko and J. Wrachtrup, "Single defect centres in diamond: A review," *physica status solidi (a)*, vol. 203, no. 13, pp. 3207–3225, 2006. DOI: https://doi.org/10.1002/pssa.200671403. eprint: https://onlinelibrary.wiley.com/doi/pdf/10.1002/pssa.200671403. [Online]. Available: https://onlinelibrary.wiley.com/doi/abs/10.1002/pssa.200671403.

[56] E. Van Oort and M. Glasbeek, "Electric-field-induced modulation of spin echoes of n-v centers in diamond," *Chemical Physics Letters*, vol. 168, no. 6, pp. 529–532, 1990, ISSN: 0009-2614. DOI: https://doi.org/10.1016/0009-2614(90)85665-Y. [Online]. Available: https://www.sciencedirect.com/science/article/pii/000926149085665Y.

[57] F. Jelezko, T. Gaebel, I. Popa, A. Gruber, and J. Wrachtrup, "Observation of coherent oscillations in a single electron spin," *Phys. Rev. Lett.*, vol. 92, p. 076 401, 7 Feb. 2004. DOI: 10.1103/PhysRevLett.92.076401. [Online]. Available: https://link.aps.org/doi/10.1103/PhysRevLett.92.076401.

[58] J. J. Sakurai and E. D. Commins, *Modern quantum mechanics, revised edition*, 1995.

[59] T. Nozaki, A. Kozioł-Rachwał, M. Tsujikawa, *et al.*, "Highly efficient voltage control of spin and enhanced interfacial perpendicular magnetic anisotropy in iridium-doped fe/mgo magnetic tunnel junctions," *NPG Asia Materials*, vol. 9, no. 12, e451–e451, 2017.

[60] D.-s. Wang, R. Wu, and A. Freeman, "First-principles theory of surface magnetocrystalline anisotropy and the diatomic-pair model," *Physical Review B*, vol. 47, no. 22, p. 14 932, 1993.

[61] S. Zhang, "Spin-dependent surface screening in ferromagnets and magnetic tunnel junctions," *Physical review letters*, vol. 83, no. 3, p. 640, 1999.

[62] M. K. Niranjan, C.-G. Duan, S. S. Jaswal, and E. Y. Tsymbal, "Electric field effect on magnetization at the fe/mgo (001) interface," *Applied Physics Letters*, vol. 96, no. 22, p. 222 504, 2010.

[63] K. Nakamura, R. Shimabukuro, Y. Fujiwara, T. Akiyama, T. Ito, and A. Freeman, "Giant modification of the magnetocrystalline anisotropy in transition-metal monolayers by an external electric field," *Physical review letters*, vol. 102, no. 18, p. 187 201, 2009.

[64] P. Ong, N. Kioussis, D. Odkhuu, P. K. Amiri, K. Wang, and G. P. Carman, "Giant voltage modulation of magnetic anisotropy in strained heavy metal/magnet/insulator heterostructures," *Physical Review B*, vol. 92, no. 2, p. 020 407, 2015.

[65] M. Liu, O. Obi, Z. Cai, *et al.*, "Electrical tuning of magnetism in fe3o4/pzn–pt multiferroic heterostructures derived by reactive magnetron sputtering," *Journal of Applied Physics*, vol. 107, no. 7, p. 073 916, 2010. DOI: 10.1063/1.3354104. eprint: https://doi.org/10.1063/1.3354104. [Online]. Available: https://doi.org/10.1063/1.3354104.

[66] A. B. Solanki, S. I. Bogdanov, A. Rustagi, *et al.*, *Electric field control of interaction between magnons and quantum spin defects*, 2021. arXiv: 2012.01497 [cond-mat.mes-hall].

[67] W. M. Itano, J. C. Bergquist, J. J. Bollinger, *et al.*, "Quantum projection noise: Population fluctuations in two-level systems," *Phys. Rev. A*, vol. 47, pp. 3554–3570, 5 May 1993. DOI: 10.1103/PhysRevA.47.3554. [Online]. Available: https://link.aps.org/doi/10.1103/PhysRevA.47.3554.